

Parameter Estimation for GW200208_22 with Targeted Eccentric Numerical-relativity Simulations

Patricia McMillin,¹ Katelyn J. Wagner,¹ Giuseppe Ficarra,² Carlos O. Lousto,¹ and R. O’Shaughnessy¹

¹*Center for Computational Relativity and Gravitation, Rochester
Institute of Technology, Rochester, New York 14623, USA*

²*Dipartimento di Fisica, Università della Calabria, Arcavacata di Rende (CS), 87036, Italy*

We have analyzed LVK gravitational wave events that show some evidence of eccentricity from TEOBResumS modeling parameter estimations and have confronted them independently with full numerical generated waveforms from our bank of nearly two thousand simulations of binary black holes. We have used RIFT for Bayesian parameter estimation and found that GW200208_22 KDE estimates favor eccentricities $e_{20} = 0.217^{+0.076}_{-0.184}$ upon entering the LVK band at ~ 20 Hz within a 90% confidence limit. Within this event analysis we employed 39 new targeted full numerical relativity simulations and we have thus found a top improved likelihood $\ln \mathcal{L}$ matching waveform, compared to model- based analysis, with an estimated eccentricity at 20Hz, $e_{20} = 0.200$, thus reinforcing the eccentric hypothesis of the binary. We have also used our full bank of numerical waveforms on GW190620 finding that it favors eccentricities in the range of $0 \leq e_{10} \leq 0.3$. New specifically targeted simulations will be required to narrow this eccentricity range.

I. INTRODUCTION

Ground-based gravitational wave (GW) detectors in the International Gravitational Wave observatory Network (IGWN), including Advanced LIGO [1] and Virgo [2], now joined by KAGRA [3] continue to identify coalescing compact binaries [4–9]. Their properties are understood by comparing gravitational wave (GW) observations to estimates of the radiation emitted from merging binary black holes, produced by detailed numerical calculations or phenomenological estimates.

Most compact binaries that enter the LIGO-Virgo-KAGRA (LVK) sensitivity band at 10Hz are expected to have quasi-circular orbits. Systems formed through isolated binary evolution form at large enough separations that their merger timescales are sufficiently large such that gravitational radiation is expected to circularize their orbit long before merger [10–12]. However, recent studies have suggested that some compact binary systems may instead display eccentric orbits, with some orbital eccentricity remaining at the time of merger. Systems with eccentric orbits may indicate an alternative formation channel, called dynamical assembly.

Binaries may form via this channel due to high rates of chance encounters in densely populated stellar environments [13], such as globular clusters [14–16], nuclear star clusters [17], or galactic centers [18], where multiple black hole interactions might be favored [19–22]. In these environments, objects that have already evolved into compact objects may encounter each other, and undergo one or a series of gravitational encounters that enable binary systems to form and merge on short timescales. These bina-

ries are expected to be short-lived, but may merge with non-negligible eccentricity that is likely measurable with current and future gravitational wave detectors [23].

There have been several recent studies that attempt to probe eccentricity in binary mergers detected by LIGO and Virgo. Romero-Shaw et al. (2020, 2021, 2022) [24–26] use an efficient reweighting method [27, 28] to obtain measurements of the orbital eccentricity for gravitational-wave sources up to and including the third LVK gravitational-wave transient catalog, GWTC-1 [5], GWTC-2.1 [8], and GWTC-3 [9]. This novel postprocessing technique first analyzes the catalog with the “proposed” spin-aligned quasi-circular waveform model **IMRPhenomD** [29], these posteriors are reweighted to the “target” model: spin-aligned eccentric waveform **SEOBNRE** [30, 31]. Results from this method are unable to distinguish between spin-induced precession and eccentricity, and are limited to moderate eccentricities at 10 Hz ($e_{10} \leq 0.2$) with restricted spins ($\chi_{\text{eff}} \leq 0.6$). Romero-Shaw et al. (2022) [32] found that GW190521, GW190620, GW191109, and GW200208_22 show considerable support for moderate eccentricity ($e_{10} \geq 0.05$) where the later two events were new additions to the population.

Gupte et al. [33] also identified GW200208_22 as eccentric from the first three LVK catalogs [5, 8, 9], as well as adding GW200129, and GW190701 to the population of events with signs of eccentricity. These results were obtained through Bayesian inference with two eccentric parameters (eccentricity and relativistic anomaly) on the LVK catalog using **DINGO** [34] with the spin-aligned quasi-circular model **SEOBNRv4HM** [35, 36] and the spin-aligned eccentric model **SEOBNRv4EHM** [37, 38]. The eccentric models used were limited to $e_{10} \leq 0.5$ and are not simulta-

neously able to include both spin-precession effects and eccentricity, thus are unable to distinguish between the two effects.

A study of the evolution of hierarchical triple systems done in [21, 22] found that scattering of the distant companion on the inner binary is more effective at imparting eccentricity onto the binary than if the companion is in a distant quasi-circular orbit. While Romero-Shaw et al. (2025) [39] completed a comparison of the properties of GW200208_22 as analyzed in [26, 33] and the astrophysical implication of this event having non-negligible eccentricity present at merger. They claim that this event almost certainly formed in a dynamical environment, where an analysis of formation scenarios for this event shows that GW200208_22 could have plausibly been formed in a hierarchical field triple or within a globular cluster but unlikely to have been the result of formation in an active galactic nucleus as it is dependent on disk geometry and the binary’s location in the disk.

Iglesias et al. [40] uses **TEOBResumS-DALI** [41–43], which can generate stable waveforms for $e \leq 0.9$ where the $e \leq 0.2$ waveforms are verified via comparison to numerical relativity waveforms, for Bayesian parameter estimation using RIFT [44]. Eccentric reanalysis on GW150914, GW190521, GW190620, GW190706, and GW190929 returned no strong preference for eccentricity for any of the events, although eccentricity can not be ruled out completely due to the lack of waveform model that simultaneously includes spin-induced precession and eccentricity.

In Healy et al. [45] using the third RIT BBH simulations catalog [46] (with $e \approx 0$) and RIFT techniques applied to LIGO/Virgo’s O1/O2 observational runs, we obtained improved binary parameters, extrinsic parameters, and the remnant properties of thirteen gravitational waves events. And then again for the first GW event in the O3 observational run, GW170729, we used the RIFT with NR waveforms approach to successfully match it in [47]. Cross-check of the RIT numerical waveforms with the completely independent SXS NR implementation for the match to the event GW150914 have been performed for up to $\ell = 5$ modes, showing a high degree of overlap and convergence toward each other’s results in [48].

Gayathri et al. (2022) [49] showed that GW190521 is most consistent with a highly eccentric black hole merger. They generated 824 targeted numerical relativity eccentric simulations, for an effective $\sim 6 \times 10^4$ gravitational waveforms with different total masses, much greater than previously available at high eccentricities. These NR simulations were compared to the observed data using RIFT [44], they found that GW190521 is best explained by a high-eccentricity, precessing model with $e \sim 0.7$.

All properties of GW190521 point to its origin being the repeated gravitational capture of black holes, making GW190521 one of the first of LIGO/Virgo’s discoveries whose formation channel is identified.

Gamba et al. (2022) [50] also analyzed GW190521 under the hypothesis of dynamical capture where the binary components are on hyperbolic orbits. They utilize **TEOBResumS** waveforms in both hyperbolic, and spin precessing flavors to perform Bayesian parameter estimation. Gamba et al. found that GW190521 favored a dynamical capture scenario with hyperbolic orbits over a quasi-circular merger. Although the exact formation scenario in the studies on GW190521 [49, 50] are distinct, both agree that this event is the result of a dynamical formation scenario.

These recent studies [24–26, 33, 39, 40, 49, 50] have identified several GW events that are potentially produced by binaries with a non-negligible orbital eccentricity entering the LVK sensitivity band. Some of the candidates deserving further study include GW190620 [25], GW191109, GW200208_22 [26], GW190701 and GW200129 [33].

This work aims to improve and build upon previous results by using model-based parameter estimation with the eccentric version of **TEOBResumS** [51] hand in hand with numerical-relativity simulations from the RIT catalog [52–55] to probe high likelihood regions of parameter space. We study in particular GW200208_22, first through parameter estimation using **TEOBResumS** with RIFT [44]. Then we generate new targeted numerical relativity simulations with the parameters of the highest likelihood models for use in parameter estimation via RIFT with the supplemented RIT catalog of simulations. This method of targeting high likelihood regions of parameter space to perform NR-based PE may potentially improve parameter estimates obtained through model-based methods. Additionally, we use the RIT catalog along with these targeted simulations to analyze GW190620 as a demonstration that our parameter space coverage allows for reasonable parameter estimates, even in the absence of specifically targeted simulations.

This paper is organized as follows. In Section II, we give an overview of our methods. In particular, in Section II A we present the numerical techniques used to produce our simulations, in Section II B we review the use of RIFT in our study, Section II C and Section II D provide the bank of simulations used and introduce the waveform model **TEOBResumS**, with focus on how eccentricity is defined, and Section II E provides the settings used for analysis. In Section III, we present the results of NR- and model-based parameter inference for GW200208_22 and GW190620, as well as a numer-

ical relativity accuracy test along with a mode-by-mode comparison of our highest likelihood simulation for GW200208.22 and a `TEOBResumS` waveform of the same parameters. In Section IV, we summarize our results and conclude with remarks on future work. Appendix A provides details on how the posterior peak and associated 90% confidence interval are calculated. Lastly, Appendix B provides the parameters of the targeted simulation produced for this work.

II. METHODS

A. Full Numerical Techniques

In order to perform the full numerical simulations of binary black holes we use the `LazEv` code [56] which employs 8th order spatial finite differences [20], 4th order Runge-Kutta time integration, and a reduced [57] Courant factor ($c = dt/dx = 1/4$).

For setting up numerical initial data for binary black holes, we regularly adopt the puncture approach [58] along with the `TWO PUNCTURES` [59] code. In order to locate apparent horizons during numerical evolutions we use the `AHFINDERDIRECT` [60] and compute horizon masses from its area A_H . Furthermore, we measure the magnitude of the horizon spins S_H , using the “isolated horizon” algorithm [61] as implemented in Ref. [62].

We also use the `CARPET` [63] mesh refinement driver to pinpoint the evolution of the black holes across the numerical domain. `CARPET` provides a “moving boxes” style of mesh refinement, where refined grids of fixed size are arranged about the coordinate centers of the holes. These grids are then moved following the trajectories of the holes during the numerical simulation.

The grid structure of our mesh refinements have a size of the largest box for typical simulations of $\pm 400M$. The number of points between 0 and 400 on the coarsest grid is XXX in nXXX (i.e. n100 has 100 points). So, the grid spacing on the coarsest level is $400/XXX$. The resolution in the wavezone is $100M/XXX$ (i.e. n100 has $M/1.00$, n120 has $M/1.2$ and n144 has $M/1.44$) and the rest of the levels are adjusted globally. For comparable masses and non-spinning black holes, the grid around one of the black holes (m_1) is fixed at $\pm 0.65M$ in size and is the 9th refinement level. Therefore the grid spacing at this highest refinement level is $400/XXX/2^8$. When considering small mass ratio binaries, we progressively add internal grid refinement levels [64]. Here we set units such that $M = m_1^H + m_2^H$ is the addition of the horizon masses.

The extraction of gravitational radiation from the

numerical relativity simulations is performed using the formulas (22) and (23) from [65] for the energy and linear momentum radiated, respectively, and the formulas in [66] for angular momentum radiated, all in terms of the extracted Weyl scalar Ψ_4 at the observer location $R_{obs} = 113M$. In order to extrapolate the observer location to infinity, we use the perturbative formulas in Ref. [67]. This extraction observer location seems to provide an acceptable accuracy for the low-medium eccentricity studies carried out in this paper, see detailed study in [68].

We perform simulations of eccentric binaries from a given initial separation corresponding to the apastron $r_p = a_r(1+e)$, by dropping the initial tangential linear momentum P_t by a factor $1-f$ from the quasi-circular one P_c at this apastron, i.e. $P_t = P_c(1-f)$. The relationship of $e(f)$ has been computed to 3.5 post-Newtonian (PN) order in [69]. To the lowest Newtonian order this relationship takes the simple form $e_0 = 2f - f^2$, and this was used to characterize eccentric simulation in the 4th release of the RIT BBH catalog [70]. Here we provide an analytic mapping to include up to 1.5 PN terms,

$$e_{1.5PN} = e_0 \left(1 + \frac{4 - e_0(\eta - 2)}{r_p} \right) + 2s_{eff} \left(3(1 - e_0) - \frac{3 + e_0^2}{\sqrt{1 - e_0}} \right) \left(\frac{M}{r_p} \right)^{\frac{3}{2}}, \quad (1)$$

where

$$s_{eff} = \frac{[(4 + 3q)\chi_1^z + q(3 + 4q)\chi_2^z]}{4(1 + q)^2}, \quad (2)$$

and $\eta = q/(1 + q)^2$ is the symmetric mass ratio, with $q = m_2/m_1$. Note that here $s_{eff} = S_{eff}/M^2$ is as derived from the PN Hamiltonian in [71] and as described in Eqs. (5)-(6), and (28)-(29) of [72], not to be confused with χ_{eff} that is rather related to $S_0/M^2 = (q\chi_2 + \chi_1)/(1 + q)$.

We will use this analytic expression of $e_{1.5PN}$ to remap the e_0 eccentricities given in the RIT BBH Catalog, then convert the $e_{1.5PN}$ eccentricity to its corresponding eccentricity at 20 Hz e_{20} using (6) for use in the parameter estimation corner plots. We also provide a direct comparison to the full $e_{3.5PN}$ eccentricity estimation for the new 39 targeted eccentric nonprecessing runs in the Appendix B.

B. RIFT

A merging compact binary can be completely characterized by its intrinsic and extrinsic parameters. The intrinsic parameters, λ , refer to the component masses, component spins, eccentricity, and

matter quantities. The seven extrinsic parameters (θ) describe the spacetime location and orientation of the system, including right ascension, declination, luminosity distance, coalescence time, inclination, orbital phase, and polarization. We will express masses in solar mass units and dimensionless non-precessing spins in terms of Cartesian components aligned with the orbital angular momentum $\chi_{i,z}$.

RIFT [44, 73, 74] is an iterative process consisting of two stages to estimate the intrinsic and extrinsic parameters of the binary source. It compares gravitational wave data d to predicted gravitational wave signals $h(\lambda, \theta)$. In the first stage, for each λ_α from some proposed “grid” $\alpha = 1, 2, \dots, N$ of candidate parameters, RIFT utilizes parallel computing to evaluate a marginal likelihood

$$\mathcal{L}_{\text{marg}}(\lambda) = \int \mathcal{L}(\lambda, \theta) p(\theta) d\theta. \quad (3)$$

from the likelihood $\mathcal{L}(\lambda, \theta)$ of the gravitational wave signal in a multi-detector network, accounting for detector response. This stage, called integrate likelihood extrinsic (ILE), provides point estimates for $\ln \mathcal{L}_{\text{marg}}(\lambda)$ using either Gaussian Process (GP) regression or random forests to interpolate a full posterior distribution over the intrinsic parameters. See the RIFT papers [44, 73, 74] for more detailed discussion.

1. Model Based RIFT

In the second iterative stage for a model-based run, RIFT first approximates $\mathcal{L}(\lambda)$ based on the set of evaluations $\{(\lambda_\alpha, \mathcal{L}_\alpha)\}$. Then, using this approximation, RIFT generates a full posterior distribution over the intrinsic parameters

$$p_{\text{post}}(\lambda) = \frac{\mathcal{L}_{\text{marg}}(\lambda) p(\lambda)}{\int d\lambda \mathcal{L}_{\text{marg}}(\lambda) p(\lambda)} \quad (4)$$

where $p(\lambda)$ is the prior on the intrinsic parameters.

The posterior is fairly sampled to generate a new grid using adaptive Monte Carlo techniques. The evaluation points and weights in that integral are weighted posterior samples, which are fairly resampled to generate conventional independent, identically distributed “posterior samples.” This second stage is called construct intrinsic posterior or CIP. For further details on RIFT’s technical underpinnings and performance, see [44, 73–75].

2. NR Based RIFT

The second phase of RIFT must be slightly different when using numerical relativity simulations as

grid points. Each NR simulation corresponds to a particular combination of the intrinsic parameters λ (mass ratio, spin components, and eccentricity) but can be scaled to any value of total mass. Therefore the second phase of RIFT instead must use a one dimensional fit to generate a refinement grid near the peak $\ln \mathcal{L}$, adaptively exploring the mass parameter space for each combination of the other intrinsic parameters which are available as NR simulations. Exploration in the other intrinsic parameters is limited to fixed points determined by which simulations are available in the catalog.

C. Simulations

The fourth release of the RIT catalog of BBH simulations [55] consists of 1881 accurate simulations, 824 in eccentric orbits with $0 < e \leq 1$, including 709 nonprecessing and 115 precessing; and 611 nonprecessing and 446 precessing quasicircular/inspiraling binary systems with mass ratios $q = m_1/m_2$ in the range $1/128 \leq q \leq 1$ and individual spins up to $\chi_i = S_i/m_i^2 = 0.95$. The catalog also provides initial parameters of the binary, trajectory information, peak radiation, and final remnant black hole properties. The catalog includes all waveform modes $l \leq 4$ of the Weyl scalar ψ_4 and the strain h (both extrapolated to null-infinity) and both are corrected for the center of mass displacement during inspiral and after merger [55].

In addition to the public RIT catalog we also use the first release of eccentric nonspinning BBH simulations covering up to 25 orbits [68]. This catalog includes 30 simulations with five eccentricities, $e \in [0, 0.45]$, and six different mass ratios, $q \in [0.11, 1.0]$. Both of these catalogs [55, 68] report initial eccentricity in terms of the eccentricity parameter, f , which results in the Newtonian definition of eccentricity $e_0 = 2f - f^2$. This measure of eccentricity can be converted to 3.5PN order using the methods described in [69], which allows for a better comparison to eccentricities reported by the model **TEOBResumS-DALI**.

D. Waveform Model

TEOBResumS [41] is an effective-one-body (EOB) model. This approach combines the phases of two-body dynamics, including inspiral, merger, and ringdown, into a single analytical method. First introduced by [76], this method allows for highly accurate waveform calculations by mapping the dynamics of a binary system onto one single, effective object that moves in the potential. The effective object is de-

scribed by equations of motion derived from general relativity. **TEOBResumS** is informed by NR simulations of BBH coalescence events for calibration and validation, particularly for the eccentric version of this model. For the model-based parameter estimation portions of this study, we use the eccentric spin-aligned waveforms from **TEOBResumS** [51] which were verified by NR for eccentricities up to $e \leq 0.3$ at 10 Hz. This model also incorporates higher order modes up to $l = |m| = 5$, except for $m = 0$. The user can also define the reference frequency for **TEOBResumS** at periastron, apastron, or the mean of both. The model-based parameter estimation runs using **TEOBResumS** for this study used the mean frequency as the reference frequency for eccentricity, whereas the NR simulations used the apastron frequency. To provide a common benchmark to directly compare the different definitions of eccentricity used in TEOB and NR, we use the **GW_ECCENTRICITY** package [77] which extracts an estimate of eccentricity from the frequency modulations of the dominant (2,2) mode. Figure 1 shows a head-to-head comparison of the frequency versus time for the (2,2) mode extracted from an NR simulation and a corresponding TEOB estimate which most resembles it; this figure's title provides the corresponding eccentricities identified by these three methods. Due to convention differences, the intrinsic TEOB parameterization adopts a higher value of its eccentricity parameter to explain this signal than the **GW_ECCENTRICITY** or NR simulation conventions, which in this case closely agree.

The version of **TEOBResumS** used in this study to provide a benchmark analysis is a previous version of the model which includes only two parameters to determine the initial conditions, e_0 and f_{ref} , to evolve the trajectories of the binary components. In the time since this analysis was performed, a new version of **TEOBResumS** has been released which includes the mean anomaly as a waveform parameter. Note that the value of the waveform eccentricity is different than the physical, time-varying eccentricity of the system, and may also mean different things depending on the choice of model.

E. Analysis

We analyze publicly available data from GWTC-2.1, and GWTC-3 [8, 9] and use the noise power spectral density curves (PSDs) associated with each specific event as part of the public data release. For GW200208.22 we used a low-frequency cutoff of 20 Hz, and for GW190620 a 10 Hz cutoff. The high frequency cutoff was 448 Hz for both GW200208.22, and GW190620. For details on the choice of high-

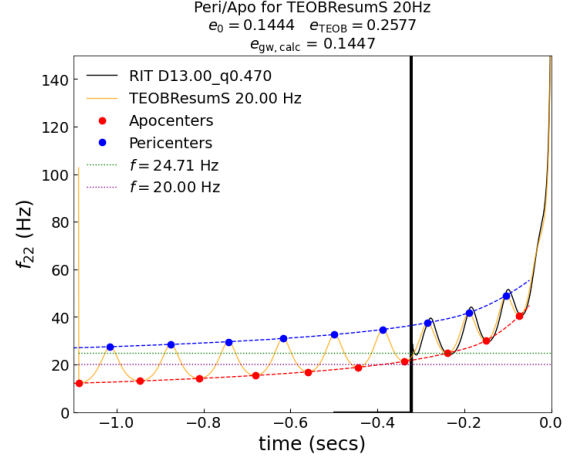


FIG. 1. We ensure that a consistent definition of eccentricity is being used, particularly for follow-up numerical relativity simulations run specifically to target points near the peak likelihoods found via model-based parameter estimation for GW200208.22. For the model-based runs, the mean value of eccentricity at the reference frequency was used, whereas the RIT simulations use eccentricity define at apoapse for a given frequency. This plot shows the values of eccentricity used by each given their particular definitions, as well as an overlap of the (2,2) mode to ensure that the shape of the waveforms match. We note that for the simulation eGW::02 the Newtonian eccentricity of $e_0 = 0.144$ translates into an eccentricity at 20 Hz of $e_{20} = 0.248$.

frequency cutoff see Appendix E of [9], and Section V of [8], respectively for each event. We adopt a uniform prior for eccentricity over the range $e \in [0.0, 0.9]$ for all events. We assume both spins are aligned with the orbital angular momentum and uniformly distributed in our prior range, which is either $|\chi_{i,z}| < 0.5$ or < 0.9 , depending on the analysis used. The more restricted spin prior is used to constrain our posteriors under the alternative assumption that the events analyzed are unlikely to be highly spinning. All other extrinsic and intrinsic priors are conventional: for example, we use a uniform prior in the detector frame masses m_i , modulo upper and lower limits in \mathcal{M}_c and q ; a Euclidean distance prior on d_L ; and conventional uninformed priors on all extrinsic angles and event time. We utilize the nonprecessing simulations, both eccentric and non-eccentric, with symmetric mass ratio $\eta = [0.2, 0.25]$ from the RIT catalog [55] as an initial grid for NR-based PE.

For the GW200208.22 event, improvement of initial NR-based PE requires targeted NR simulations, these simulations have the intrinsic parameters of the highest $\ln \mathcal{L}_{\text{marg}}$ points of model-based PE with spins in the range $\chi_{i,z} = \pm 0.4$. These targeted simulations are constructed using the same techniques

as [68], which differ slightly from the techniques described in Section II A. To further fill in the NR simulation grid in e_0 and χ_{eff} space, we add simulations of fixed $q = 0.5$, $\chi_{2,i} = 0$ at two values of eccentricity, $e_0 = 0.1, 0.19$, with seven values of $\chi_{1,z} \in [0.1 - 0.6]$. In addition two more simulations are added to fill a void in the grid in q and e_0 space, with positive spin in m_1 , eccentricity of 0.04, and mass ratios of 0.6, and 0.7.

The parameters of these additional simulations are provided in Table III and Table IV with the targeted simulations labeled eGW::01-23, additional simulations in (e_0, χ_{eff}) space labeled eGW::24-37, and additional simulations in (q, e_0) space labeled eGW::38-39. The catalog of 30 eccentric nonspinning simulations covering up to 25 orbits [68] is employed in the resolution study in Section III C, as well as to further fill in the grid of simulations for NR-based PE in Section III.

III. ANALYSIS OF ACTUAL EVENTS

In this section we present the results of the eccentric reanalysis of GW200208.22 and GW190620 using direct comparison to numerical relativity. These events were analyzed based on prior evidence or indications of eccentricity [25, 26, 33]. While in the discussion below we exclusively employ comparisons to numerical relativity simulations, for context we also provide a comparison model-based results in Section III B.

A. GW200208.22

The LVK collaboration identified in GWTC-3 [9] the low SNR event $(7.4^{+1.4}_{-1.2})$ GW200208.22 as an event with high-mass sources, where the component masses, mass ratio and chirp mass in the detector frame as reported in [78] are: $m_1 = 83.4^{+171.8}_{-48.7}$, $m_2 = 21.9^{+13.0}_{-11.8}$, $q = 0.21^{+0.67}_{-0.16}$, and $\mathcal{M}_c = 31.3^{+26.2}_{-8.5}$. This event also has significant support for positive effective spin with a 95% probability that $\chi_{\text{eff}} > 0$ where the reported effective spin from Table IV of [9] is $\chi_{\text{eff}} = 0.45^{+0.43}_{-0.44}$.

Figure 2 shows our analysis of GW200208.22 using direct comparison to nonprecessing numerical relativity simulations, as described in Section II E. While our underlying catalog of nonprecessing eccentric NR simulations has only a few simulations which have optimal e and χ_{eff} , our catalog and thus analysis specifically includes followup simulations targeted at the expected binary parameters. Looking first at the marginal likelihoods derived by comparing each NR simulation against the data, the

best-fitting numerical relativity simulations for this event are all somewhat eccentric, and many indicate modest aligned spin. Conversely, the most eccentric simulations in our catalog consistently fit poorly, suggesting the eccentricity is very likely below $e_0 \simeq 0.3$. Similarly, none of the best fitting simulations have negative χ_{eff} , suggesting a preference for positive spin, and most of the best fitting simulations have modest mass ratio $q > 0.4$.

Interpolating these sparsely sampled marginal likelihoods versus mass, aligned spins, and eccentricity, we infer a joint posterior distribution for these parameters. Keeping in mind potential systematic errors introduced by our coverage, we would estimate that the binary mass ratio posterior favors a binary with moderately asymmetric components, where the maximum of a kernel density estimate (KDE) on the 1-dimensional posteriors have reasonable agreement for results derived using the priors $|\chi_{i,z}| < 0.5$ and $|\chi_{i,z}| < 0.9$, $q = 0.532^{+0.237}_{-0.108}$ and $q = 0.529^{+0.226}_{-0.099}$ respectively, where the maximum KDE value is reported with the symmetric 90% confidence interval on the 1D posterior; the details of constructing the maximum KDE value and its errors are further described in Appendix A. Similarly, the marginal eccentricity posterior seems to robustly favor modest eccentricity, $e_{20} = 0.217^{+0.076}_{-0.184}$ for $|\chi_{i,z}| < 0.5$ and $e_{20} = 0.209^{+0.111}_{-0.192}$ for $|\chi_{i,z}| < 0.9$ and bound it above ($e_{20} \lesssim 0.3$), for both spin priors. The χ_{eff} posterior is centered on zero effective spin with a slight preference for positive spin for both choices of prior peaking at $\chi_{\text{eff}} = 0.241^{+0.133}_{-0.299}$ and $\chi_{\text{eff}} = 0.265^{+0.449}_{-0.469}$ for the priors $|\chi_{i,z}| < 0.5$ and $|\chi_{i,z}| < 0.9$ respectively. For both choices of spin prior, the chirp mass posterior has a maximum at $\mathcal{M}_c = 27.217^{+18.444}_{-2.668} M_\odot$ for $|\chi_{i,z}| < 0.5$ and $\mathcal{M}_c = 27.558^{+13.740}_{-2.761} M_\odot$ for $|\chi_{i,z}| < 0.9$. We obtain similar parameter values for mass ratio q , detector frame chirp mass \mathcal{M}_c , and effective spin χ_{eff} as the LVK reported values [9, 78].

Figure 3 shows an analysis of GW200208.22 using direct comparison to precessing, both eccentric and noneccentric, numerical relativity simulations, based on a comparison to the simulations provided in [55]. This analysis was completed with the same settings as the nonprecessing analysis but with additional triangular priors on the remaining spin components $|\chi_{i,x}| < 0.99$ and $|\chi_{i,y}| < 0.99$, as well as a triangular prior for the in-plane spin components, $\chi_{i,\perp} \in [0, 1]$. Where the in-plane spin components are defined as

$$\chi_{i,\perp} = \left| \frac{\mathbf{S}_i}{m_i^2} \times \hat{\mathbf{L}} \right|. \quad (5)$$

The marginal likelihoods obtained through direct comparison of each NR simulation to the data in

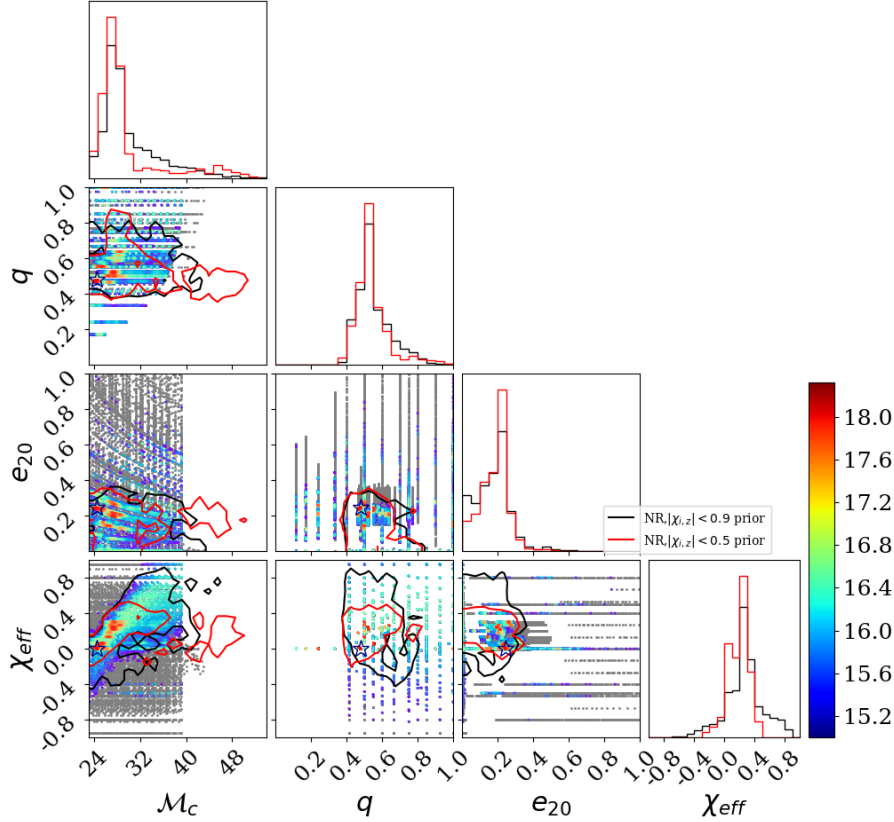


FIG. 2. A corner plot showing the results of NR based PE for GW200208.22 with a grid consisting of the RIT catalog [55], targeted NR simulations (parameters provided in Appendix B), and eccentric non-spinning simulations [68]. Two posteriors are shown with different χ_{eff} priors, $|\chi_{i,z}| < 0.9$ (black) and $|\chi_{i,z}| < 0.5$ (red). The colorbar represents the value of $\ln \mathcal{L}_{\text{marg}}$ and a star is placed at the peak $\ln \mathcal{L}$ simulation, these are present on all corner plots.

this secondary precessing analysis, reveal the best-fitting numerical relativity simulations are nonspinning and mildly eccentric. Still some simulations with marginal likelihoods just below the best-fitting simulations have anti-aligned spins indicating spin-induced precession may be present in the binary. Just as in the nonprecessing analysis the best fitting simulations all have mass ratio $q > 0.4$ and many have positive χ_{eff} , suggesting a preference for positive spin.

Now we look at the joint posteriors generated by interpolating the marginal likelihoods versus mass, aligned spins, eccentricity, and the precession parameter $\chi_{1,\perp}$. The chirp mass and mass ratio posteriors generally agree with the nonprecessing analysis with a maximum near $\mathcal{M}_c = 29.451^{+16.175}_{-4.341} M_\odot$ and $q = 0.746^{+0.178}_{-0.320}$ respectively. The χ_{eff} posterior now has a maximum near zero effective spin with a preference for positive effective spin with a maximum at $\chi_{\text{eff}} = 0.421^{+0.263}_{-0.480}$. The marginal eccentricity posterior is again bounded above at $e_{20} \lesssim 0.3$, but in the precessing analysis the maximum is at

$e_{20} = 0.013^{+0.209}_{-0.012}$. Seemingly this is due to the abundance of precessing simulations with $e_{20} = 0$. Finally the $\chi_{1,\perp}$ posterior favors modest transverse spin, peaking at $\chi_{1,\perp} = 0.464^{+0.343}_{-0.353}$.

B. Discussion of GW200208.22: differences between models and NR

Figure 4 shows a comparison of the inferred posteriors from numerical relativity PE and model-based PE. The results of the direct comparison of GW200208.22 to nonprecessing numerical relativity simulations, presented in Section III A, along with the $|\chi_{i,z}| < 0.9$ spin prior were used to construct the joint posterior distribution of the masses, aligned spins, and eccentricity. In conjunction, a model-based parameter estimation was performed using `TEOBResumS-DALI` with the same priors as Section II E, except for the spin prior which is $|\chi_{i,z}| < 0.99$.

It is clear that the posteriors generated from mod-

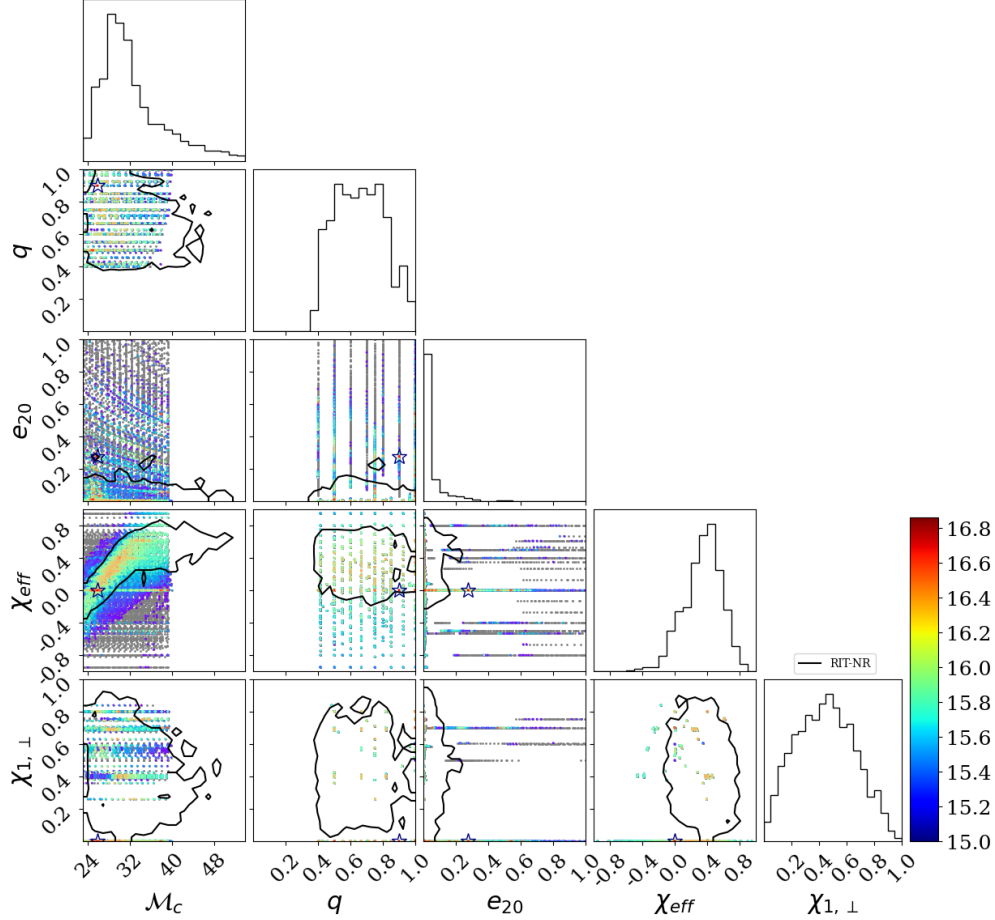


FIG. 3. A corner plot showing the results of NR based PE for GW200208.22 including precession parameter $\chi_{1,\perp}$ with a grid consisting of the RIT catalog [55]. The posterior fit is generated using the priors described in Section II E with an additional triangular prior on the precession parameter $\chi_{1,\perp}$.

els and NR agree quite well, as both methods favor a modest eccentricity, with the posterior of model-based PE peaking at $e_{\text{TEOB}} = 0.197^{+0.082}_{-0.119}$ and bound it above at $e_{\text{TEOB}} \lesssim 0.3$. The χ_{eff} posteriors are almost identical, for both methods they are centered on zero effective spin with a slight preference for positive effective spin as the model-based posterior peaks at $\chi_{\text{eff}} = 0.191^{+0.234}_{-0.224}$. Similarly, the chirp mass posteriors for both model-based and NR-based PE return a similar maximum, with the model peaking at $\mathcal{M}_c = 26.680^{+4.300}_{-2.049} M_\odot$. Finally, both posteriors favor a binary with moderately asymmetric components as there is strong support for $q > 0.4$ with the model-based PE maximum at $q = 0.568^{+0.354}_{-0.272}$.

Figure 5 demonstrates the difference in how f_{ref} and eccentricity are defined for the numerical relativity simulations and the model **TEOBResumS-DALI**. The RIT NR simulations are constructed using a reference frequency defined at the apoapsis, this warrants that all waveform's higher frequencies will be

included, while **TEOBResumS-DALI** constructs waveforms with the mean of the apoapsis and periapsis frequencies as its reference. Our **TEOBResumS-DALI** models used in analysis for GW200208.22 have a mean reference frequency of 20 Hz, this happened to correspond to the apoapsis frequency of 24.45 Hz used to construct the NR simulations, see Figure 1. Thus plotting a model with a reference frequency that numerically matches the NR reference frequency does not result in a matching frequency over time curve, as seen by mismatch of the model with a mean reference frequency of $f_{\text{ref}} = 24.45\text{Hz}$ and the NR simulation in the left panel of Figure 5. We must ensure that the reference frequency used for generating models and NR waveforms are equivalent by converting the mean frequency used in **TEOBResumS-DALI** to an apoapsis frequency for use in the NR simulations. Taking the conversion into account results in a better match of frequency versus time for a model with a mean reference frequency of

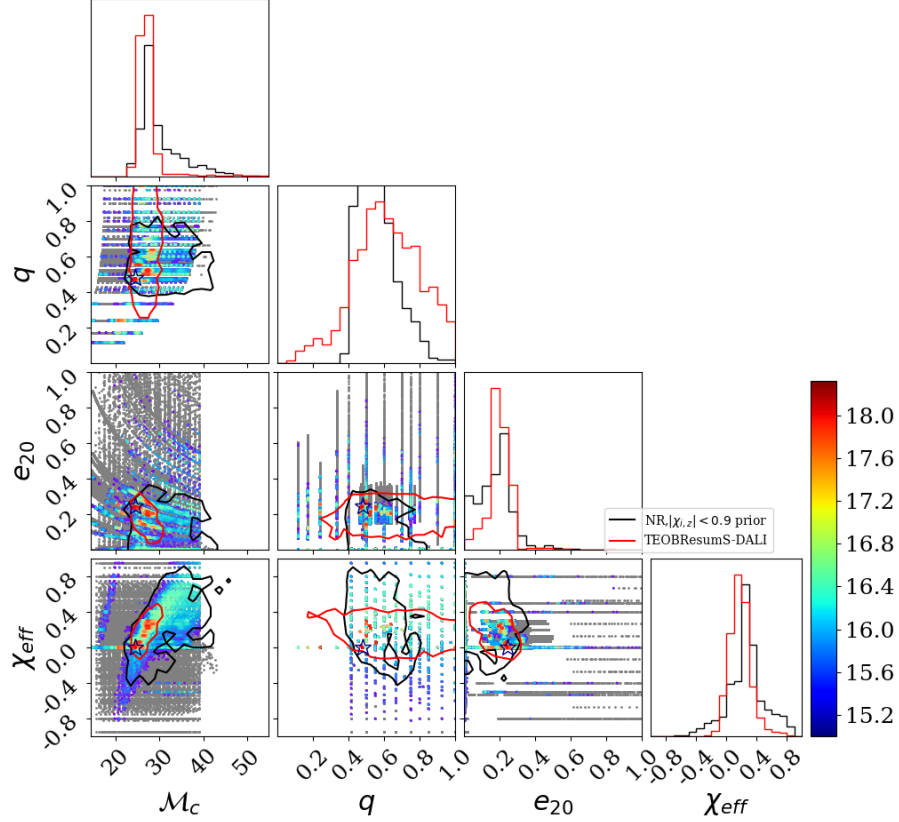


FIG. 4. Model-based parameter estimation using RIFT with TEOBResumS-DALI (red posterior) for event GW200208-22. NR-based PE using RIFT with all simulations described in Section II E (black posterior and grid points). This event shows strong support for non-zero eccentricity, with a posterior maximum near $e_{20} \sim 0.2$ and very little support for $e_{20} = 0$. Note that the TEOBResumS-DALI posterior has eccentricity defined as e_{TEOB} but is plotted on the e_{20} axis. We use a mean reference frequency of $f_{ref} = 20\text{Hz}$ and eccentricity defined at this reference frequency.

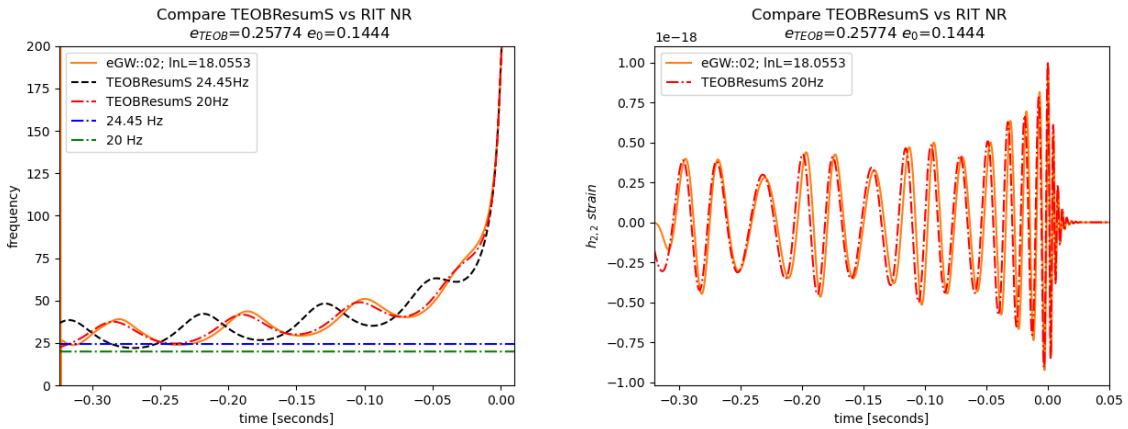


FIG. 5. Comparison of frequency vs time (left), and $h_{2,2}$ strain vs time (right) for highest $\ln \mathcal{L}$ targeted simulation for GW200208-22 (eGW::02) and TEOBResumS models with the same intrinsic parameters. The left panel demonstrates the difference in reference frequency definition, NR defines the reference frequency at apoapsis while TEOBResumS models uses the mean value of periapsis and apoapsis frequencies. The mean frequency of 20 Hz is equivalent to the frequency 24.45 Hz at apoapsis. The right panel shows the (2,2) mode GW strain of eGW::02 and the corresponding TEOBResumS with $f_{ref} = 20\text{Hz}$.

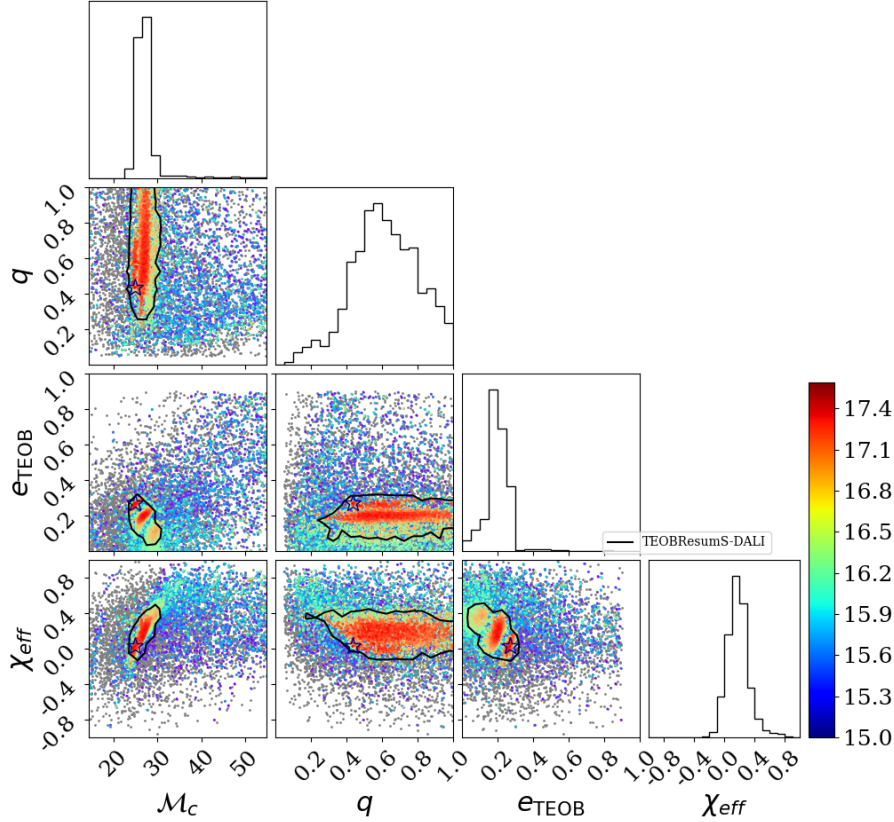


FIG. 6. Model-based parameter estimation using RIFT with TEOBResumS-DALI for event GW200208_22.

$f_{ref} = 20\text{Hz}$ and the NR simulation.

In addition to the change in frequency plot, we look at the $(2,2)$ -mode strain for a model with a 20 Hz mean reference frequency and the corresponding NR simulation in the right panel of Figure 5. The model-based waveform and the NR waveform exhibit a good match during the inspiral phase and align nearly perfectly in the merger and ringdown phases. Further demonstrating that a reference frequency of 20 Hz defined as the mean of apoapsis and periapsis frequencies is equivalent to the 24.45 Hz frequency for this simulation at apoapsis, that the NR simulations use.

We show in Figure 6 the model-based PE done with TEOBResumS-DALI, the posterior shown is the same as the red curve in Figure 4 along with the underlying marginal likelihoods derived by comparing TEOBResumS-DALI models against the data. This plot demonstrates the key difference when performing NR and model-based PE, models can be easily generated at any set of intrinsic parameters, while NR simulations are restricted to the set of intrinsic parameters at which they were generated, with the exception that they can be scaled to any value of total mass. Additionally, the peak marginal likelihood

points obtained from model-based PE are slightly lower than the marginal likelihoods of the same points obtained through NR-based PE. The slight improvement in marginal likelihood values may be due in part to the nature of how the NR simulations are constructed, as they are able to return more accurate waveforms for the higher order modes. We examine this possibility with a mode by mode comparison of the peak targeted simulation (eGW::02). In order to visualize the potential differences between TEOBResumS modeling and full numerical waveforms we display in Fig. 7 the comparison of the leading $\ell = 2, 3$ modes with the top targeted simulation eGW::02. From this we observe that the key differences are not localized in any particular mode but rather in the generic higher accuracy of NR waveforms. We also recall here the studies made in [48] where it was found (See Fig. 3 there) that the completely different implementation of the full numerical solution to the two black hole problem, such as those of RIT and SXS, agree with each other by two orders of magnitude closer than each of them with the SEOB model for the targeted runs of the first event GW150914.

We are able to directly compare these peak like-

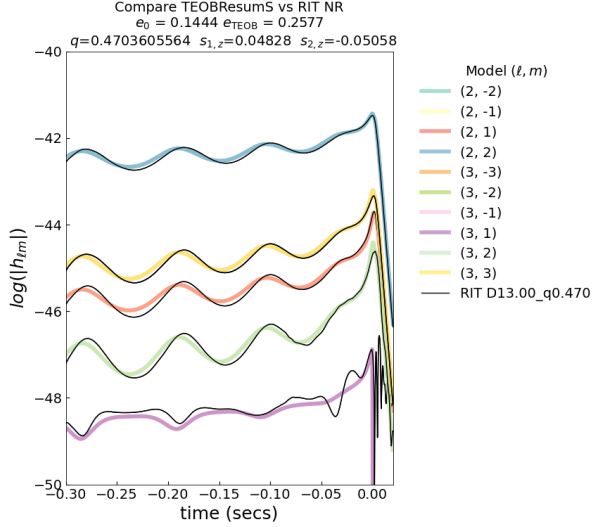


FIG. 7. In addition to the (2,2) mode, we examine higher order modes to view a mode-by-mode comparison between the highest likelihood NR simulation (shown in black) with a TEOBResumS waveform generated with the highest likelihood parameter estimation results shown mode-by-mode in the colored lines. We do this in particular to examine whether some differences in the waveform may cause the NR simulations to return slightly higher $\ln \mathcal{L}$ values than the models. We note that for the simulation eGW::02 the Newtonian eccentricity of $e_0 = 0.144$ is equivalent to the eccentricity at 20 Hz of $e_{20} = 0.248$.

likelihoods due to the method we employed during the targeting stage of our analysis, whereby we generated simulations at the intrinsic parameters of the peak marginal likelihood points from the model-based PE. Exact intrinsic parameters and associated maximum marginal likelihoods found through a gaussian process fit for the simulations with $\ln \mathcal{L} \geq 17$ in the ILE stage of RIFT are given in Table I, where likelihoods from both NR- and model-based PE are provided for only the targeted simulations due to the method we employed to generate targeted simulations. For the peak likelihood simulations generated through other means (without the input from model-based analysis) there are no points from the model-based analysis with equivalent intrinsic parameters for comparison with the NR-based analysis likelihoods.

To eliminate possible data conditioning effects present due to the manner in which the NR simulations are loaded for use in RIFT, we perform a gaussian process fit on the simulations presented in Table I and Table II. We rerun each simulation with the same settings as described in Section II E but with the use of a denser initial grid in chirp mass with ten times the points, where the bounds are ± 2

of each simulations chirp mass. The gaussian process fit is performed on the output from the first stage of RIFT (ILE), we first perform a cut in marginal log-likelihood, by only considering the data points that fall within 2 of the maximum $\ln \mathcal{L}$, then we fit the marginal likelihoods as a function of chirp mass. We employ an additive kernel composed of a white noise kernel with variance 8×10^{-5} plus the product of a constant kernel with value 0.5 and the radial basis function kernel with length scale set at 2 times the standard deviation of chirp mass. We then compute the mean prediction of the GP fit and its 90% confidence interval, then report the maximum $\ln \mathcal{L}$ of the fit and its associated chirp mass. The results of this fitting method for eBBH::08 at resolution n120 are shown in Figure 8, where the maximum log-likelihood and its 90% confidence interval of the GP fit is 18.658 ± 0.029 at a chirp mass of $24.433 M_\odot$.

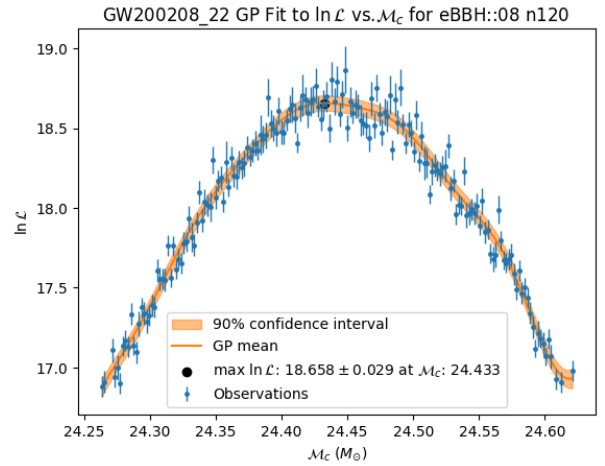


FIG. 8. Gaussian Process fit for the top matching simulation (eBBH::08) at resolution n120 for event GW200208.22. RIFT data points and their errors from the ILE stage are shown in blue. The mean prediction of the GP fit is given by the orange curve, and its 90% confidence interval shaded in orange. The maximum $\ln \mathcal{L}$ of the GP mean and its 90% confidence interval is given by the black point.

Since the NR simulations benefits from the total mass M invariance, we would only know the physical scale after the matching to a specific signal is performed. We can then *a posteriori* evaluate the eccentricity at a standard value, such as 20 Hz, from its reference NR value. In order to do so, we use the formulas for the eccentricity evolution at the lowest post-Newtonian order from [79], Eq. (5.11), to

TABLE I. Peak marginal likelihood, $\ln \mathcal{L}_{\text{marg}}$, NR simulations and models of GW200208_22, where all have the dimensionless spin components $s_1^x = s_1^y = s_2^x = s_2^y = 0$ and $\ln \mathcal{L} \geq 17$ as reported from the ILE stage of RIFT. The likelihood values reported in the NR_PE $\ln \mathcal{L}$ column are a result of gaussian process fitting discussed in Section III B. For the targeted simulations generated from the peak $\ln \mathcal{L}$ points in model-based analysis, the model-based eccentricity e_{TEOB} and likelihoods are provided. For simulations not generated from the model-based analysis (eBBH::08, eGW::26, eGW::36) these values are unable to be provided and denoted by $-$ in the e_{TEOB} and model_PE $\ln \mathcal{L}$ columns. The NR starting frequency, $f_{\text{ref}}^{\text{NR}}$, is the frequency at apoapsis which corresponds to the mean frequency of $f_{\text{ref}} = 20$ Hz used by TEOBResumS-DALI, see Figure 1. e_{20} is the conversion of the initial 3.5PN order eccentricity, $e_{3.5\text{PN}}$, to 20 Hz. Simulation eBBH::08 is EccBBH::08 from [68].

| NR_sim_id | m_1/M_\odot | m_2/M_\odot | $q = m_2/m_1$ | s_1^z | s_2^z | $e_{3.5\text{PN}}$ | e_{20} | e_{TEOB} | model_PE $\ln \mathcal{L}$ | NR_PE $\ln \mathcal{L}$ | NR f_{ref} (Hz) |
|-----------|---------------|---------------|---------------|---------|---------|--------------------|----------|-------------------|-------------------------------|----------------------------|-----------------------------|
| eBBH::08 | 41.162 | 19.659 | 0.478 | 0 | 0 | 0.241 | 0.200 | – | – | 18.658 | 15.22 |
| eGW::02 | 41.160 | 19.360 | 0.470 | 0.0483 | -0.0506 | 0.216 | 0.248 | 0.258 | 17.338 | 18.005 | 24.45 |
| eGW::04 | 43.798 | 22.778 | 0.520 | 0.2180 | 0.2931 | 0.203 | 0.221 | 0.201 | 17.153 | 17.784 | 22.48 |
| eGW::08 | 39.386 | 21.786 | 0.553 | 0.2812 | -0.3379 | 0.212 | 0.242 | 0.271 | 17.087 | 17.406 | 24.33 |
| eGW::06 | 43.824 | 22.953 | 0.524 | 0.3446 | -0.0214 | 0.204 | 0.222 | 0.208 | 17.392 | 17.485 | 22.54 |
| eGW::07 | 38.604 | 21.366 | 0.553 | -0.0007 | 0.1314 | 0.213 | 0.246 | 0.272 | 17.009 | 17.405 | 24.69 |
| eGW::26 | 43.417 | 21.708 | 0.500 | 0.2000 | 0 | 0.139 | 0.152 | – | – | 17.078 | 22.34 |
| eGW::36 | 45.118 | 22.560 | 0.500 | 0.4501 | 0 | 0.267 | 0.288 | – | – | 16.977 | 22.58 |

obtain

$$e(20\text{Hz}) = e_{\text{NR}} \left(\frac{f_{\text{ref}}^{\text{NR}}}{20\text{Hz}} \right)^{19/18}, \quad (6)$$

valid for small eccentricities and in the inspiral post-Newtonian regime of the binary.

An expression for generic values of the eccentricity and including higher post-Newtonian order can be derived from [79], eq. (5.11), for the evolution of the eccentricity with the semimajor axis a , and its relation to the orbital frequency from [80], Eq. (4.13),

$$a(e_{20})/a(e_{\text{NR}}) = r(f_{\text{ref}}^{\text{NR}})/r(20\text{Hz}). \quad (7)$$

This implicit transcendental equation for e_{20} can be then solved numerically. We thus provided a conversion of the $e_{3.5\text{PN}}$ eccentricity at the beginning of the NR simulation into the corresponding eccentricity e_{20} at 20 Hz in Table I.

C. Evaluation of Numerical Relativity accuracy

The targeted NR simulations have been designed with the numerical grid structure and base n120 resolution optimized for catalog production as studied in [68]. In order to evaluate the accuracy of this reference numerical set up to match the gravitational wave signals detected by the LVK collaboration, we perform successive lower and higher global resolution (otherwise identical) simulations of eBBH::08, the top matching waveform of GW200208_22. The

results of evaluating $\ln \mathcal{L}$ for these full numerical resolutions n100, n120, n144, n172 and n208, corresponding to global factors of 1.2 increases, are displayed in Table II. We first note that the deviations of $\ln \mathcal{L}$ from its n120 reference remain well within a fraction of a tenth of a percent and over an order of magnitude less than the differences we observe among the different targeted simulations in Table I. We also provide in Table II a direct comparison of the waveforms at different resolutions by computing their overlap over the whole range of the simulations as given by the matching measure,

$$\mathcal{M} \equiv \frac{\langle h_1 | h_2 \rangle}{\sqrt{\langle h_1 | h_1 \rangle \langle h_2 | h_2 \rangle}}, \quad (8)$$

as implemented via a complex overlap as described in Eq. (2) in Ref. [81]:

$$\langle h_1 | h_2 \rangle = 2 \max_t \left| \int_{-\infty}^{\infty} \frac{d\omega e^{i\omega t}}{S_n(\omega)} [\tilde{h}_1(\omega) \tilde{h}_2(\omega)^*] \right|, \quad (9)$$

where $\tilde{h}(\omega)$ is the Fourier transform of $h(t)$ and $S_n(\omega)$ is the power spectral density of the detector noise (here specifically taken $S_n(\omega) = 1$ since we are interested in the direct waveforms comparisons). We adopt the leading modes $(\ell, m) = (2, 2)$ of ψ_4 for the computations and we do not maximize over an overall constant time shift and an overall constant phase shift.

Figure 9 displays the highest marginalized log-likelihood NR waveform (top candidate eBBH::08 in Table I) overlaid with whitened strain data near GW200208_22 detector response in the LIGO Hanford (H1) and Livingston (L1) instruments. We note that the fit here displays nearly 10 waveform cycles

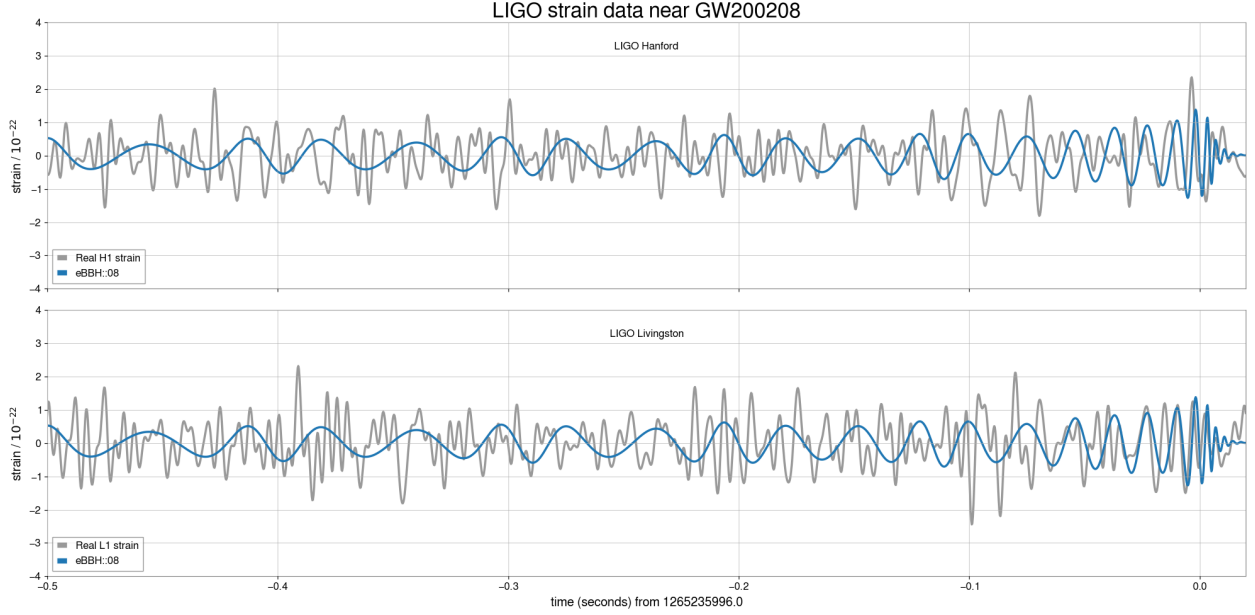


FIG. 9. Best fitting time-domain NR waveform (eBBH::08) overlaid on whitened strain data near GW200208.22.

TABLE II. $\ln \mathcal{L}$ and matching for the peak likelihood NR simulation (eBBH::08) of GW200208.22. The likelihood values reported here are a result of gaussian process fitting discussed in Section III B.

| Resolution | $\ln \mathcal{L}$ | $\Delta(\ln \mathcal{L})$ | matching |
|------------|-------------------|---------------------------|----------|
| n100 | 18.659 | -0.010 | 0.971862 |
| n120 | 18.658 | -0.011 | 0.999576 |
| n144 | 18.653 | -0.016 | 0.994080 |
| n172 | 18.676 | +0.007 | 0.999890 |
| n208 | 18.669 | 0.000 | 1.000000 |

before the binary black hole merger and thus contributes to the case of eccentric mergers with more of an inspiral orbit in the LIGO band compared to the other strong case for eccentric merger, GW19051, as this is much more massive [49] than GW200208.22.

D. GW190620

The LVK collaboration identified in GWTC-2.1 [8] GW190620 an event with $\text{SNR } 12.1^{+0.3}_{-0.4}$ where the component masses, mass ratio and chirp mass in the detector frame as reported in [82] are: $m_1 = 84.6^{+20.0}_{-15.4}$, $m_2 = 53.1^{+17.1}_{-19.7}$, $q = 0.62^{+0.33}_{-0.27}$, and $\mathcal{M}_c = 57.6^{+9.0}_{-11.2}$. This event also has significant support for positive effective spin where the reported effective spin from Table VI of [8] is $\chi_{\text{eff}} = 0.33^{+0.22}_{-0.25}$.

Figure 10 shows the results of parameter inference for GW190620, using direct comparison to the

bank of nonprecessing numerical relativity simulations described in Section II E. Unlike in the case of GW200208.22, numerical relativity simulations specifically targeted for this event were not generated as part of the analysis for GW190620. This was done to demonstrate that the bank of simulations described in Section II E provides sufficient coverage of parameter space to return reasonable parameter estimates.

We first look at the marginal likelihoods computed from the comparison of each NR simulation against the data. For this event all of the best-fitting numerical relativity simulations are somewhat eccentric, with many having moderate aligned spin. Again, the highly eccentric simulations in our catalog consistently fit the data poorly, indicating that eccentricity is likely bounded below $e_{10} \lesssim 0.3$. Likewise, most of the best fitting simulations exhibit a modest mass ratio $q > 0.4$, and none of the best fitting simulations have negative χ_{eff} , implying a preference for positive spin.

These sparsely sampled marginal likelihoods are interpolated over mass, aligned spins, and eccentricity resulting in an inferred joint posterior distribution for these parameters. Noting that potential systematic errors may have been introduced by our coverage, we estimate that the binary mass ratio posterior favors a binary with moderately asymmetric masses, peaking at $q = 0.535^{+0.160}_{-0.082}$ and $q = 0.620^{+0.129}_{-0.264}$, respectively for results obtained using the two spin priors, $|\chi_{i,z}| < 0.5$ and $|\chi_{i,z}| < 0.9$. The marginal eccentricity posterior is bounded above

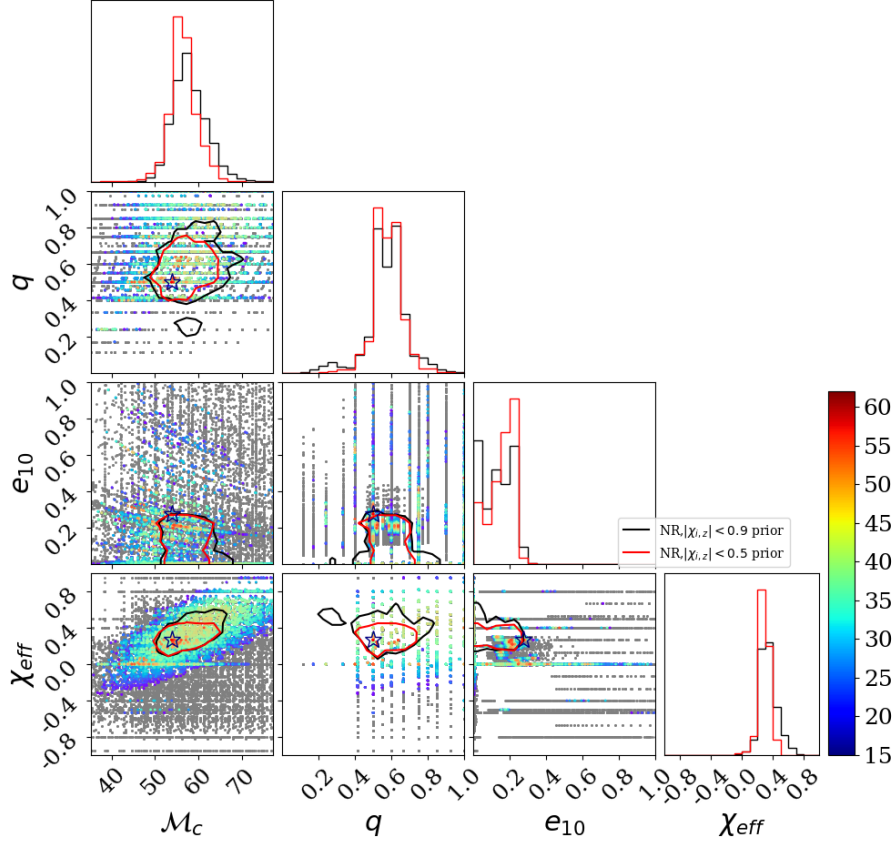


FIG. 10. A corner plot showing the results of NR based PE for GW190620 using all available RIT NR simulations described in Section II E. Two posteriors are shown with different spin priors, $|\chi_{i,z}| < 0.9$ (black) and $|\chi_{i,z}| < 0.5$ (red). We provide eccentricity at the reference frequency for this event of 10 Hz, which is found by using (6) with 10 Hz in the denominator in place of 20 Hz.

by $e_{10} \lesssim 0.3$ with moderate support for a modest non-zero eccentricity, with the posterior maximum near $e_{10} = 0.204^{+0.022}_{-0.197}$ for the restricted spin prior ($|\chi_{i,z}| < 0.5$) while $e_{10} = 0.205^{+0.033}_{-0.201}$ for the less restricted spin prior ($|\chi_{i,z}| < 0.9$). These eccentricity posteriors, while they have a nonzero maximum, still have significant support near zero that may be resolved by applying a similar targeting treatment as we did for GW200208_22. For both choices of spin prior the posterior on χ_{eff} favors positive effective spin, with a maximum at $\chi_{\text{eff}} = 0.281^{+0.117}_{-0.109}$ for the $|\chi_{i,z}| < 0.5$ prior and $\chi_{\text{eff}} = 0.295^{+0.256}_{-0.106}$ for the $|\chi_{i,z}| < 0.9$ prior, which is consistent with [8, 25]. For both choices of spin prior, the chirp mass posterior has a maximum at $\mathcal{M}_c = 55.876^{+6.109}_{-4.412} M_\odot$ for the spin prior $|\chi_{i,z}| < 0.5$ and $\mathcal{M}_c = 57.367^{+7.743}_{-5.182} M_\odot$ for the spin prior $|\chi_{i,z}| < 0.9$. We obtain parameter values with reasonable agreement for mass ratio q , detector frame chirp mass \mathcal{M}_c , and effective spin χ_{eff} to the LVK reported values [8, 82].

IV. CONCLUSIONS AND DISCUSSION

The use of the available bank of simulations in the 4th RIT catalog [55] developed in part for targeting the event GW190521 [49] with eccentric precessing simulations, provides us with the opportunity to assess the possibility of exploring new eccentric BBH entering the LVK sensitivity band from 10-20Hz on. We have thus applied it to GW200208_22 finding a KDE distribution clearly favoring eccentricity over quasicircular simulations as displayed in Fig. 11. Independently we have used current waveform models, such as **TEOBResumS** [41] to estimate the highest likelihood $\ln \mathcal{L}$ region in the binary's parameter space. We then compared those waveforms with precisely the corresponding targeted full numerical simulations systematically finding better matching for the later to the GW signal as displayed in Table I. In addition, we have covered the targeted region of parameter space with additional 39 new simulations searching for a new high $\ln \mathcal{L}$. Notably, by also us-

ing the 30 recently simulated eccentric waveforms in [68] we have found a simulation with an even higher likelihood than any of the 39 targeted simulations.

In summary, we have found strong support to the second case (after GW190521) of clear non negligible eccentricity in a BBH entering the sensitivity band of LVK with the studies performed on GW200208.22. This result is supported by waveform models and independently by our full numerical simulations of merging black holes. Those full numerical eccentric waveforms prove to be an even better match to the GW200208.22 signal as measured by the likelihood $\ln \mathcal{L}$ on the targeted simulations as displayed in Table I.

Even more interesting is the case that notwithstanding the targeted simulations are a better match to the GW signals than their corresponding models, since those simulations have been chosen to target the highest likelihood region of parameter space provided by the models, it may occur that one could find an even better matching set of parameters in their neighborhood (still within the 90% confidence limit) that would lead to an even higher $\ln \mathcal{L}$. Such seems to be the case here, since an eccentric simulation, among the 30 nonspinning previously performed in [68], labeled as EccBBH::08, with parameters $q = 0.4776$ and initial separation $D/M = 19.26$ lead to the outstanding highest value of almost $\ln \mathcal{L} \approx 18.7$ (See Table I). Notably, for this simulation the initial eccentricity is given by $e_{3.5PN} = 0.241$ (with $e_{20} = 0.200$). The remnant properties of the final merged hole for this EccBBH::08 simulation are given in Table VIII of Appendix A of Ref. [68].

We note that in Table I the top $\ln \mathcal{L}$ simulations for GW200208.22 are eccentric nonprecessing simulations while the precessing simulations, eccentric or not, in our catalog fell below, in $\ln \mathcal{L}$ terms, as can be seen by the respective colorbar maximum values in Fig. 2 vs. Fig 3. While for GW190620, the case of precession might be more relevant, and thus requiring specifically targeted simulations to match to its gravitational wave signal.

The success of our purely numerical techniques encourage the targeting of other GW events with new simulations in an effort to improve their parameter estimates. Among other interesting cases of BBH carrying non negligible eccentricity into the LVK sensitivity band to study are GW190620 as well as revisiting GW190521 to seek improvements in its parameters. We also note the recent study of other potentially eccentric GW signals in [83] identified using phenomenological models.

ACKNOWLEDGMENTS

This material is based upon work supported by NSF's LIGO Laboratory which is a major facility fully funded by the National Science Foundation. COL gratefully acknowledges support from NSF awards AST-2319326 and PHY-2207920. ROS gratefully acknowledges support from NSF awards PHY-1912632, PHY-2012057, PHY-2309172, AST-2206321, and the Simons Foundation.

Appendix A: Kernel Density Estimates and Errors

The 1-dimensional posteriors shown on the diagonal of each corner plot (Figures 2–4, 6, and 10) can be used as the basis to generate kernel density estimates (KDE) for each parameter. We first use the posterior samples that RIFT outputs in its second stage (CIP) for each intrinsic parameter, $p_{\text{post}}(\lambda)$, to construct a KDE using `scipy.stats.gaussian_kde` with equally weighted datapoints with weight $1/N$ where N is set to the number of posterior samples, 2000. Resultant KDEs are evaluated on a grid half the size of the posterior samples over each parameter's respective range, $e \in [0, 1]$, $q \in [0, 1]$, $\chi_{\text{eff}} \in [-1, 1]$, and \mathcal{M}_c range consistent with the analysis in Section III. The maximum of the KDE evaluated over each grid is reported as the point with the highest density, this represents the maximum parameter value for each intrinsic parameter's 1-dimensional posterior. Errors of this maximum value are reported as the 90% confidence interval of the 1-dimensional posterior. We note that the maximum parameters as reported from the KDE analysis are not the same as the parameters for the peak likelihood simulations in Table I. The maximum KDE parameters are determined through the analysis of the full posterior over the intrinsic parameters, constructed in the CIP stage of RIFT, while the parameters reported in Table I are just the intrinsic parameters of the simulation where their likelihoods are evaluated in the ILE stage of RIFT. Thus the key difference here is the inclusion of the intrinsic prior, the KDE analysis of the full intrinsic posterior takes our priors into account while the values of Table I do not. As a result we expect a difference between the parameters of the peak $\ln \mathcal{L}$ simulations in Table I and the maximum of the 1-dimensional posteriors for each intrinsic parameter found through the KDE analysis. As a demonstration of the method the resultant KDE and maximum parameter value is shown overlaid with the 1-dimensional posterior histogram for the eccentricity of the NR-based PE of GW200208.22 in Figure 11.

We assess the errors of the maximum parameter value by generating 1000 additional posterior realizations, where the real posterior samples are resampled by choosing random rows from the real posterior samples with replacement such that our resampled posterior is the same size as the real posterior samples. For each posterior sample realization the KDE is computed then evaluated on the same grid as used for the real posterior sample, and the same maximum finding process is applied. The standard deviation and the symmetric 90% confidence interval on the set of maximum parameter

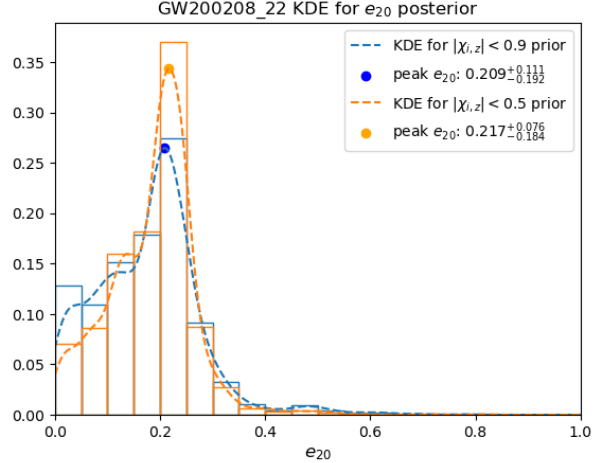


FIG. 11. Kernel density estimate of the GW200208.22 NR-based PE 1-dimensional eccentricity posterior (histograms from Figure 2) for the two different spin priors, $|\chi_{i,z}| < 0.9$ (blue) and $|\chi_{i,z}| < 0.5$ (orange). The maximum of the KDE for each prior is indicated by a dot of the same color.

values is computed where these errors represent the statistical error for the maximum parameter value obtained through the KDE. For instance, the standard deviation of the location of the maximum eccentricity found in Figure 11 are 0.210 ± 0.002 for the $|\chi_{i,z}| < 0.9$ prior and 0.218 ± 0.002 for the $|\chi_{i,z}| < 0.5$ prior. The 90% confidence interval on the set of maximum eccentricity values in Figure 11 are $0.210^{+0.003}_{-0.004}$ for the $|\chi_{i,z}| < 0.9$ prior and $0.218^{+0.003}_{-0.004}$ for the $|\chi_{i,z}| < 0.5$ prior. Similarly, errors on the other maximum intrinsic parameters (χ_{eff} , \mathcal{M}_c , q , etc.) are on the same order of magnitude, which indicates that the statistical error in the KDE maximum finding method is negligible.

Appendix B: NR simulation parameters

Here we provide the details of the simulations specifically performed for the studies in this paper, in addition to the 1881 simulations in the fourth RIT catalog [55] and the additional 30 simulations in [68].

In Table III a small P_r component has been added to the initial quasicircular parameters from the instantaneous P_t up to 3.5PN radiation terms [84, 85] in order to ensure a lower eccentricity. In all other explicit eccentric cases the prescription consists on setting $P_r = 0$ [69].

In Table IV we provide the merged black hole properties, final mass, spin and recoil velocity of the remnant hole. We also provide a measure of the radiated gravitational energy, consistent with

TABLE III. Initial data parameters for the sequence of simulations described in Sec.IIC with a larger black hole (labeled 1) and a smaller black hole (labeled 2). Punctures are located at $\vec{r}_1 = (x_1, 0, 0)$ and $\vec{r}_2 = (x_2, 0, 0)$ with mass ratio $q = m_2^H/m_1^H$, eccentricity parameter f , linear momenta $\vec{P} = \pm(0, P_t, 0)$, puncture masses m^p/M , horizon (Christodoulou) masses m^H/M , dimensionless spin parameter χ and total ADM mass M_{ADM}/M . We also provide initial values of the Newtonian eccentricity $e_0 = 2f - f^2$ and PN orders estimates.

| Run | x_1/M | x_2/M | q | f | P_t/M | m_1^p/M | m_2^p/M | m_1^H/M | m_2^H/M | χ_1 | χ_2 | M_{ADM}/M | e_0 | $e_{1.5\text{PN}}$ | $e_{3.5\text{PN}}$ |
|---------|---------|---------|-------|-------|---------|-----------|-----------|-----------|-----------|----------|----------|--------------------|-------|--------------------|--------------------|
| eGW::01 | 4.12 | -8.88 | 0.465 | 0.075 | 0.0641 | 0.6567 | 0.3078 | 0.6826 | 0.3174 | 0.2482 | 0.0335 | 0.9915 | 0.144 | 0.187 | 0.207 |
| eGW::02 | 4.16 | -8.84 | 0.470 | 0.075 | 0.0650 | 0.6706 | 0.3101 | 0.6801 | 0.3199 | 0.0483 | -0.0506 | 0.9915 | 0.144 | 0.191 | 0.216 |
| eGW::03 | 4.40 | -8.60 | 0.512 | 0.075 | 0.0663 | 0.6290 | 0.3288 | 0.6613 | 0.3387 | 0.2926 | -0.0256 | 0.9912 | 0.144 | 0.187 | 0.206 |
| eGW::04 | 4.45 | -8.55 | 0.520 | 0.075 | 0.0664 | 0.6361 | 0.3205 | 0.6579 | 0.3421 | 0.2180 | 0.2930 | 0.9912 | 0.144 | 0.185 | 0.203 |
| eGW::05 | 4.46 | -8.54 | 0.523 | 0.075 | 0.0667 | 0.6323 | 0.3313 | 0.6564 | 0.3436 | 0.2367 | 0.1360 | 0.9912 | 0.144 | 0.186 | 0.205 |
| eGW::06 | 4.46 | -8.54 | 0.524 | 0.075 | 0.0666 | 0.6147 | 0.3339 | 0.6563 | 0.3437 | 0.3445 | -0.0214 | 0.9911 | 0.144 | 0.186 | 0.204 |
| eGW::07 | 4.63 | -8.37 | 0.553 | 0.075 | 0.0684 | 0.6343 | 0.3439 | 0.6437 | 0.3563 | -0.0007 | 0.1314 | 0.9910 | 0.144 | 0.190 | 0.213 |
| eGW::08 | 4.62 | -8.38 | 0.553 | 0.075 | 0.0683 | 0.6137 | 0.3296 | 0.6439 | 0.3561 | 0.2812 | -0.3379 | 0.9911 | 0.144 | 0.190 | 0.212 |
| eGW::09 | 4.71 | -8.29 | 0.570 | 0.075 | 0.0686 | 0.6051 | 0.3481 | 0.6371 | 0.3629 | 0.2942 | -0.1823 | 0.9910 | 0.144 | 0.188 | 0.208 |
| eGW::10 | 4.76 | -8.24 | 0.579 | 0.075 | 0.0694 | 0.6227 | 0.3531 | 0.6334 | 0.3666 | 0.0678 | -0.1531 | 0.9909 | 0.144 | 0.192 | 0.216 |
| eGW::11 | 4.80 | -8.20 | 0.586 | 0.075 | 0.0688 | 0.5927 | 0.3591 | 0.6304 | 0.3696 | 0.3287 | 0.0573 | 0.9909 | 0.144 | 0.185 | 0.203 |
| eGW::12 | 4.86 | -8.14 | 0.599 | 0.075 | 0.0694 | 0.5850 | 0.3622 | 0.6255 | 0.3745 | 0.3448 | -0.1223 | 0.9908 | 0.144 | 0.187 | 0.206 |
| eGW::13 | 4.88 | -8.12 | 0.602 | 0.075 | 0.0694 | 0.5932 | 0.3655 | 0.6243 | 0.3757 | 0.2895 | 0.0222 | 0.9908 | 0.144 | 0.186 | 0.205 |
| eGW::14 | 4.95 | -8.05 | 0.617 | 0.075 | 0.0696 | 0.5762 | 0.3709 | 0.6184 | 0.3816 | 0.3557 | 0.0560 | 0.9907 | 0.144 | 0.185 | 0.202 |
| eGW::15 | 4.97 | -8.03 | 0.619 | 0.075 | 0.0700 | 0.5967 | 0.3705 | 0.6175 | 0.3825 | 0.2108 | 0.0759 | 0.9907 | 0.144 | 0.187 | 0.207 |
| eGW::16 | 5.01 | -7.99 | 0.629 | 0.075 | 0.0700 | 0.5711 | 0.3758 | 0.6140 | 0.3860 | 0.3599 | 0.0042 | 0.9907 | 0.144 | 0.186 | 0.203 |
| eGW::17 | 5.03 | -7.97 | 0.632 | 0.075 | 0.0701 | 0.5845 | 0.3724 | 0.6128 | 0.3872 | 0.2730 | 0.1722 | 0.9907 | 0.144 | 0.186 | 0.203 |
| eGW::18 | 5.05 | -7.95 | 0.635 | 0.075 | 0.0703 | 0.5782 | 0.3783 | 0.6114 | 0.3886 | 0.3059 | 0.0048 | 0.9907 | 0.144 | 0.187 | 0.205 |
| eGW::19 | 5.06 | -7.94 | 0.637 | 0.075 | 0.0703 | 0.5776 | 0.3784 | 0.6107 | 0.3893 | 0.3048 | 0.0639 | 0.9907 | 0.144 | 0.186 | 0.204 |
| eGW::20 | 5.06 | -7.94 | 0.638 | 0.075 | 0.0701 | 0.5604 | 0.3787 | 0.6106 | 0.3894 | 0.3962 | 0.0584 | 0.9907 | 0.144 | 0.184 | 0.201 |
| eGW::21 | 5.20 | -7.80 | 0.668 | 0.075 | 0.0710 | 0.5607 | 0.3902 | 0.5994 | 0.4006 | 0.3407 | 0.0286 | 0.9906 | 0.144 | 0.185 | 0.203 |
| eGW::22 | 5.54 | -7.46 | 0.744 | 0.075 | 0.0723 | 0.5556 | 0.4034 | 0.5735 | 0.4265 | 0.1841 | 0.2711 | 0.9904 | 0.144 | 0.186 | 0.203 |
| eGW::23 | 5.66 | -7.34 | 0.772 | 0.075 | 0.0728 | 0.5374 | 0.4250 | 0.5644 | 0.4356 | 0.2708 | 0.0186 | 0.9904 | 0.144 | 0.187 | 0.206 |
| eGW::24 | 4.33 | -8.67 | 0.500 | 0.050 | 0.0680 | 0.6548 | 0.3236 | 0.6667 | 0.3333 | 0.1000 | 0.0000 | 0.9917 | 0.098 | 0.128 | 0.141 |
| eGW::25 | 4.33 | -8.67 | 0.500 | 0.050 | 0.0679 | 0.6515 | 0.3236 | 0.6667 | 0.3333 | 0.1500 | 0.0000 | 0.9917 | 0.098 | 0.127 | 0.140 |
| eGW::26 | 4.33 | -8.67 | 0.500 | 0.050 | 0.0677 | 0.6468 | 0.3236 | 0.6667 | 0.3333 | 0.2000 | 0.0000 | 0.9917 | 0.098 | 0.126 | 0.139 |
| eGW::27 | 4.33 | -8.67 | 0.500 | 0.050 | 0.0675 | 0.6329 | 0.3236 | 0.6667 | 0.3333 | 0.3000 | 0.0000 | 0.9917 | 0.098 | 0.125 | 0.137 |
| eGW::28 | 4.33 | -8.67 | 0.500 | 0.050 | 0.0673 | 0.6124 | 0.3236 | 0.6667 | 0.3333 | 0.4000 | 0.0000 | 0.9917 | 0.098 | 0.124 | 0.135 |
| eGW::29 | 4.33 | -8.67 | 0.500 | 0.050 | 0.0671 | 0.5993 | 0.3236 | 0.6667 | 0.3333 | 0.4500 | 0.0000 | 0.9917 | 0.098 | 0.123 | 0.134 |
| eGW::30 | 4.32 | -8.68 | 0.500 | 0.050 | 0.0668 | 0.5450 | 0.3236 | 0.6667 | 0.3333 | 0.6000 | 0.0000 | 0.9917 | 0.098 | 0.122 | 0.131 |
| eGW::31 | 4.33 | -8.67 | 0.500 | 0.100 | 0.0644 | 0.6549 | 0.3237 | 0.6667 | 0.3333 | 0.1000 | 0.0000 | 0.9909 | 0.190 | 0.251 | 0.285 |
| eGW::32 | 4.33 | -8.67 | 0.500 | 0.100 | 0.0643 | 0.6516 | 0.3237 | 0.6667 | 0.3333 | 0.1500 | 0.0000 | 0.9909 | 0.190 | 0.250 | 0.282 |
| eGW::33 | 4.33 | -8.67 | 0.500 | 0.100 | 0.0642 | 0.6469 | 0.3237 | 0.6667 | 0.3333 | 0.2000 | 0.0000 | 0.9909 | 0.190 | 0.248 | 0.279 |
| eGW::34 | 4.33 | -8.67 | 0.500 | 0.100 | 0.0639 | 0.6330 | 0.3237 | 0.6667 | 0.3333 | 0.3000 | 0.0000 | 0.9909 | 0.190 | 0.246 | 0.274 |
| eGW::35 | 4.32 | -8.68 | 0.500 | 0.100 | 0.0637 | 0.6125 | 0.3238 | 0.6667 | 0.3333 | 0.4000 | 0.0000 | 0.9909 | 0.190 | 0.244 | 0.269 |
| eGW::36 | 4.32 | -8.68 | 0.500 | 0.100 | 0.0636 | 0.5994 | 0.3238 | 0.6667 | 0.3333 | 0.4500 | 0.0000 | 0.9909 | 0.190 | 0.242 | 0.267 |
| eGW::37 | 4.32 | -8.68 | 0.500 | 0.100 | 0.0633 | 0.5451 | 0.3238 | 0.6667 | 0.3333 | 0.6000 | 0.0000 | 0.9908 | 0.190 | 0.239 | 0.260 |
| eGW::38 | 4.87 | -8.13 | 0.600 | 0.025 | 0.0731 | 0.5889 | 0.3647 | 0.6250 | 0.3750 | 0.3200 | 0.0000 | 0.9917 | 0.049 | 0.063 | 0.068 |
| eGW::39 | 5.35 | -7.65 | 0.700 | 0.025 | 0.0755 | 0.5500 | 0.4012 | 0.5882 | 0.4118 | 0.3400 | 0.0000 | 0.9914 | 0.049 | 0.063 | 0.068 |

the final mass of the merged hole and waveform properties such as the peak luminosity, amplitude and frequency of the leading (2,2)-mode. The time and number of orbits to merger of our simula-

tions completed the table. These properties are given in the format of the metadata in the RIT BBH waveforms catalog <https://ccrgpages.rit.edu/~RITCatalog/>.

- [1] J. Aasi *et al.*, Class. Quant. Grav. **32**, 074001 (2015).
[2] F. Acernese *et al.*, Class. Quant. Grav. **32**, 024001 (2015).

- [3] T. Akutsu, M. Ando, K. Arai, Y. Arai, S. Araki, A. Araya, N. Aritomi, Y. Aso, S. Bae, Y. Bae, L. Baiotti, R. Bajpai, M. A. Barton, K. Cannon, E. Capocasa, M. Chan, C. Chen, K. Chen, Y. Chen,

TABLE IV. Properties of the sequence of simulations described in Sec.IIC. We report the remnant mass M_f/M and spin χ_f , the radiated energy $\delta\mathcal{M} = M_{\text{ADM}} - M_f$, merger time t_m/M , number of orbits N , strain peak amplitude $(r/M)|h_{22}^{\text{peak}}|$, recoil velocity V_{kick} , peak frequency $M\omega_{22}^{\text{peak}}$ and peak luminosity $\mathcal{L}_{\text{peak}}$.

| Run | M_f/M | χ_f | $\delta\mathcal{M}/M$ | t_m/M | N | $V_{\text{kick}}[\text{km/s}]$ | $(r/M) h_{22}^{\text{peak}} $ | $M\omega_{22}^{\text{peak}}$ | $\mathcal{L}_{\text{peak}}[10^{-56}\text{erg/s}]$ |
|---------|---------|----------|-----------------------|---------|-------|--------------------------------|-------------------------------|------------------------------|---|
| eGW::01 | 0.9574 | 0.6946 | 0.0341 | 1291.5 | 8.22 | 97.21 | 0.3355 | 0.3594 | 2.9193 |
| eGW::02 | 0.9620 | 0.6241 | 0.0295 | 1115.6 | 7.17 | 138.34 | 0.3337 | 0.3457 | 2.6316 |
| eGW::03 | 0.9543 | 0.7157 | 0.0370 | 1267.5 | 8.11 | 76.37 | 0.3492 | 0.3663 | 3.2155 |
| eGW::04 | 0.9538 | 0.7125 | 0.0374 | 1302.8 | 8.34 | 107.35 | 0.3479 | 0.3660 | 3.1797 |
| eGW::05 | 0.9539 | 0.7105 | 0.0372 | 1267.9 | 8.11 | 92.05 | 0.3518 | 0.3659 | 3.2322 |
| eGW::06 | 0.9528 | 0.7320 | 0.0384 | 1295.2 | 8.31 | 65.62 | 0.3489 | 0.3684 | 3.2745 |
| eGW::07 | 0.9580 | 0.6466 | 0.0331 | 1093.1 | 7.04 | 143.03 | 0.3542 | 0.3512 | 2.9670 |
| eGW::08 | 0.9562 | 0.6973 | 0.0349 | 1140.4 | 7.38 | 76.56 | 0.3551 | 0.3596 | 3.1904 |
| eGW::09 | 0.9539 | 0.7153 | 0.0371 | 1187.2 | 7.65 | 67.23 | 0.3627 | 0.3648 | 3.4162 |
| eGW::10 | 0.9507 | 0.7347 | 0.0401 | 1216.9 | 7.81 | 58.00 | 0.3692 | 0.3708 | 3.6142 |
| eGW::11 | 0.9498 | 0.7402 | 0.0410 | 1266.8 | 8.13 | 57.15 | 0.3635 | 0.3714 | 3.5460 |
| eGW::12 | 0.9572 | 0.6541 | 0.0338 | 1041.8 | 6.70 | 101.51 | 0.3639 | 0.3496 | 3.1338 |
| eGW::13 | 0.9506 | 0.7309 | 0.0402 | 1225.9 | 7.88 | 59.30 | 0.3695 | 0.3707 | 3.6047 |
| eGW::14 | 0.9483 | 0.7494 | 0.0425 | 1266.8 | 8.15 | 49.12 | 0.3682 | 0.3733 | 3.6674 |
| eGW::15 | 0.9514 | 0.7202 | 0.0394 | 1199.6 | 7.70 | 73.55 | 0.3724 | 0.3663 | 3.5945 |
| eGW::16 | 0.9482 | 0.7479 | 0.0425 | 1247.6 | 8.03 | 49.62 | 0.3718 | 0.3729 | 3.7094 |
| eGW::17 | 0.9485 | 0.7399 | 0.0422 | 1248.4 | 8.02 | 61.94 | 0.3722 | 0.3718 | 3.6762 |
| eGW::18 | 0.9494 | 0.7368 | 0.0413 | 1215.0 | 7.82 | 51.03 | 0.3749 | 0.3715 | 3.7142 |
| eGW::19 | 0.9486 | 0.7406 | 0.0420 | 1231.1 | 7.91 | 51.36 | 0.3746 | 0.3725 | 3.7327 |
| eGW::20 | 0.9469 | 0.7604 | 0.0437 | 1282.1 | 8.26 | 44.67 | 0.3695 | 0.3751 | 3.7412 |
| eGW::21 | 0.9474 | 0.7480 | 0.0432 | 1227.8 | 7.90 | 44.79 | 0.3788 | 0.3746 | 3.8399 |
| eGW::22 | 0.9466 | 0.7422 | 0.0438 | 1206.8 | 7.78 | 66.17 | 0.3873 | 0.3727 | 3.9463 |
| eGW::23 | 0.9483 | 0.7361 | 0.0421 | 1158.8 | 7.50 | 35.60 | 0.3876 | 0.3698 | 3.8918 |
| eGW::24 | 0.9592 | 0.6563 | 0.0325 | 1616.2 | 9.28 | 124.28 | 0.3469 | 0.3534 | 2.9266 |
| eGW::25 | 0.9580 | 0.6710 | 0.0337 | 1651.5 | 9.49 | 113.40 | 0.3457 | 0.3547 | 2.9632 |
| eGW::26 | 0.9572 | 0.6857 | 0.0345 | 1689.4 | 9.74 | 100.06 | 0.3435 | 0.3580 | 2.9887 |
| eGW::27 | 0.9552 | 0.7185 | 0.0365 | 1770.0 | 10.23 | 78.68 | 0.3453 | 0.3661 | 3.1732 |
| eGW::28 | 0.9521 | 0.7487 | 0.0396 | 1845.0 | 10.66 | 63.72 | 0.3466 | 0.3733 | 3.3564 |
| eGW::29 | 0.9508 | 0.7630 | 0.0409 | 1883.2 | 10.91 | 57.21 | 0.3445 | 0.3764 | 3.3939 |
| eGW::30 | 0.9458 | 0.8095 | 0.0459 | 2002.9 | 11.67 | 54.34 | 0.3478 | 0.3948 | 3.7727 |
| eGW::31 | 0.9595 | 0.6523 | 0.0314 | 790.1 | 5.74 | 124.18 | 0.3396 | 0.3502 | 2.7935 |
| eGW::32 | 0.9591 | 0.6704 | 0.0318 | 828.4 | 5.98 | 113.27 | 0.3414 | 0.3577 | 2.8920 |
| eGW::33 | 0.9579 | 0.6888 | 0.0330 | 863.2 | 6.18 | 95.92 | 0.3466 | 0.3598 | 3.0655 |
| eGW::34 | 0.9543 | 0.7191 | 0.0366 | 921.0 | 6.53 | 83.00 | 0.3493 | 0.3639 | 3.2444 |
| eGW::35 | 0.9524 | 0.7463 | 0.0384 | 984.0 | 7.02 | 58.36 | 0.3413 | 0.3716 | 3.2240 |
| eGW::36 | 0.9517 | 0.7633 | 0.0392 | 1020.4 | 7.27 | 57.75 | 0.3419 | 0.3781 | 3.3437 |
| eGW::37 | 0.9451 | 0.8085 | 0.0458 | 1119.0 | 7.92 | 55.30 | 0.3489 | 0.3890 | 3.7663 |
| eGW::38 | 0.9504 | 0.7364 | 0.0413 | 2266.9 | 11.91 | 55.95 | 0.3671 | 0.3705 | 3.5854 |
| eGW::39 | 0.9477 | 0.7465 | 0.0437 | 2205.0 | 11.62 | 44.90 | 0.3808 | 0.3743 | 3.8539 |

H. Chu, Y. K. Chu, S. Eguchi, Y. Enomoto, R. Flaminio, Y. Fujii, M. Fukunaga, M. Fukushima, G. Ge, A. Hagiwara, S. Haino, K. Hasegawa, H. Hayakawa, K. Hayama, Y. Himemoto, Y. Hiranuma, N. Hirata, E. Hirose, Z. Hong, B. H. Hsieh, C. Z. Huang, P. Huang, Y. Huang, B. Ikenoue, S. Inam, K. Inayoshi, Y. Inoue, K. Ioka, Y. Itoh, K. Izumi, K. Jung, P. Jung, T. Kajita, M. Kamiizumi, N. Kanda, G. Kang, K. Kawaguchi, N. Kawai, T. Kawasaki, C. Kim, J. C. Kim, W. S. Kim, Y. M. Kim, N. Kimura, N. Kita, H. Kitazawa, Y. Kojima, K. Kokeyama, K. Komori, A. K. H. Kong, K. Kotake, C. Kozakai, R. Kozu, R. Kumar, J. Kume, C. Kuo, H. S. Kuo, S. Kuroyanagi, K. Kusayanagi, K. Kwak, H. K. Lee, H. W. Lee,

R. Lee, M. Leonardi, L. C. C. Lin, C. Y. Lin, F. L. Lin, G. C. Liu, L. W. Luo, M. Marchio, Y. Michimura, N. Mio, O. Miyakawa, A. Miyamoto, Y. Miyazaki, K. Miyo, S. Miyoki, S. Morisaki, Y. Moriwaki, K. Nagano, S. Nagano, K. Nakamura, H. Nakano, M. Nakano, R. Nakashima, T. Narikawa, R. Negishi, W. T. Ni, A. Nishizawa, Y. Obuchi, W. Ogaki, J. J. Oh, S. H. Oh, M. Ohashi, N. Ohishi, M. Ohkawa, K. Okutomi, K. Oohara, C. P. Ooi, S. Oshino, K. Pan, H. Pang, J. Park, F. E. P. Arellano, I. Pinto, N. Sago, S. Saito, Y. Saito, K. Sakai, Y. Sakai, Y. Sakuno, S. Sato, T. Sato, T. Sawada, T. Sekiguchi, Y. Sekiguchi, S. Shibagaki, R. Shimizu, T. Shimoda, K. Shimode, H. Shinkai, T. Shishido, A. Shoda, K. Somiya,

- E. J. Son, H. Sotani, R. Sugimoto, T. Suzuki, T. Suzuki, H. Tagoshi, H. Takahashi, R. Takahashi, A. Takamori, S. Takano, H. Takeda, M. Takeda, H. Tanaka, K. Tanaka, K. Tanaka, T. Tanaka, T. Tanaka, S. Tanioka, E. N. Tapia San Martin, S. Telada, T. Tomaru, Y. Tomigami, T. Tomura, F. Travasso, L. Trozzo, T. Tsang, K. Tsubono, S. Tsuchida, T. Tsuzuki, D. Tuyenbayev, N. Uchikata, T. Uchiyama, A. Ueda, T. Uehara, K. Ueno, G. Ueshima, F. Uraguchi, T. Ushiba, M. H. P. M. van Putten, H. Vocca, J. Wang, C. Wu, H. Wu, S. Wu, W. R. Xu, T. Yamada, K. Yamamoto, K. Yamamoto, T. Yamamoto, K. Yokogawa, J. Yokoyama, T. Yokozawa, T. Yoshioka, H. Yuzurihara, S. Zeidler, Y. Zhao, and Z. H. Zhu, *Progress of Theoretical and Experimental Physics* **2021**, 05A101 (2021), arXiv:2005.05574 [physics.ins-det].
- [4] B. Abbott et al. (The LIGO Scientific Collaboration and the Virgo Collaboration), *Phys. Rev. Lett* **116**, 061102 (2016).
- [5] B. Abbott et al. (The LIGO Scientific Collaboration and the Virgo Collaboration), *Phys. Rev. X* **6**, 041015 (2016), arXiv:1606.04856 [gr-qc].
- [6] The LIGO Scientific Collaboration, the Virgo Collaboration, B. P. Abbott, R. Abbott, T. D. Abbott, F. Acernese, K. Ackley, C. Adams, T. Adams, P. Addesso, and et al., *Phys. Rev. Lett* **119**, 161101 (2017).
- [7] R. Abbott, T. D. Abbott, S. Abraham, F. Acernese, K. Ackley, A. Adams, C. Adams, R. X. Adhikari, V. B. Adya, C. Affeldt, and et al., *Astrophysical Journal* **915**, L5 (2021), arXiv:2106.15163 [astro-ph.HE].
- [8] R. Abbott, T. D. Abbott, F. Acernese, K. Ackley, C. Adams, N. Adhikari, R. X. Adhikari, V. B. Adya, C. Affeldt, D. Agarwal, and et al., *Phys. Rev. D* **109**, 022001 (2024).
- [9] R. Abbott, T. D. Abbott, F. Acernese, K. Ackley, C. Adams, N. Adhikari, R. X. Adhikari, V. B. Adya, C. Affeldt, D. Agarwal, and et al., *Physical Review X* **13**, 041039 (2023), arXiv:2111.03606 [gr-qc].
- [10] H. A. Bethe and G. E. Brown, *The Astrophysical Journal* **506**, 780–789 (1998).
- [11] K. Belczynski, V. Kalogera, and T. Bulik, *The Astrophysical Journal* **572**, 407–431 (2002).
- [12] S. Stevenson, A. Vigna-Gómez, I. Mandel, J. W. Barrett, C. J. Neijssel, D. Perkins, and S. E. de Mink, *Nature Communications* **8** (2017), 10.1038/ncomms14906.
- [13] I. Mandel and R. O’Shaughnessy, *Classical and Quantum Gravity* **27**, 114007 (2010).
- [14] A. Sadowski *et al.*, *Astrophys. J.* **676**, 1162 (2008), arXiv:0710.0878 [astro-ph].
- [15] C. L. Rodriguez, P. Amaro-Seoane, S. Chatterjee, and F. A. Rasio, *Phys. Rev. Lett.* **120**, 151101 (2018).
- [16] M. Zevin, J. Samsing, C. Rodriguez, C.-J. Haster, and E. Ramirez-Ruiz, *Astrophysical Journal* **871** (2019), 10.3847/1538-4357/aaf6ec.
- [17] G. Fragione and J. Silk, *Monthly Notices of the Royal Astronomical Society* **498**, 4591 (2020), <https://academic.oup.com/mnras/article-pdf/498/4/4591/33798574/staa2629.pdf>.
- [18] J. Samsing, M. MacLeod, and E. Ramirez-Ruiz, *The Astrophysical Journal* **784**, 71 (2014).
- [19] M. Campanelli, C. O. Lousto, and Y. Zlochower, *Phys. Rev. D* **77**, 101501(R) (2008), arXiv:0710.0879 [gr-qc].
- [20] C. O. Lousto and Y. Zlochower, *Phys. Rev. D* **77**, 024034 (2008), arXiv:0711.1165 [gr-qc].
- [21] G. Ficarra, A. Ciarfella, and C. O. Lousto, *Phys. Rev. D* **108**, 064045 (2023), arXiv:2308.07365 [gr-qc].
- [22] G. Ficarra and C. O. Lousto, *Phys. Rev. D* **110**, 084072 (2024), arXiv:2406.11985 [gr-qc].
- [23] C. L. Rodriguez, P. Amaro-Seoane, S. Chatterjee, K. Kremer, F. A. Rasio, J. Samsing, C. S. Ye, and M. Zevin, *Phys. Rev. D* **98**, 123005 (2018).
- [24] I. Romero-Shaw, P. D. Lasky, E. Thrane, and J. C. Bustillo, *The Astrophysical Journal Letters* **903**, L5 (2020).
- [25] I. Romero-Shaw, P. D. Lasky, and E. Thrane, *Astrophysical Journal* **921**, L31 (2021).
- [26] I. M. Romero-Shaw, P. D. Lasky, and E. Thrane, *Astrophys. J.* **940**, 171 (2022), arXiv:2206.14695 [astro-ph.HE].
- [27] I. M. Romero-Shaw, P. D. Lasky, and E. Thrane, *Monthly Notices of the Royal Astronomical Society* **490**, 5210–5216 (2019).
- [28] E. Payne, C. Talbot, and E. Thrane, *Phys. Rev. D* **100**, 123017 (2019).
- [29] S. Khan, S. Husa, M. Hannam, F. Ohme, M. Pürrer, X. Jiménez Forteza, and A. Bohé, *Phys. Rev. D* **93**, 044007 (2016), arXiv:1508.07253 [gr-qc].
- [30] Z. Cao and W.-B. Han, *Phys. Rev. D* **96**, 044028 (2017).
- [31] X. Liu, Z. Cao, and L. Shao, *Phys. Rev. D* **101**, 044049 (2020).
- [32] I. Romero-Shaw, P. D. Lasky, and E. Thrane, *The Astrophysical Journal* **940**, 171 (2022).
- [33] N. Gupte *et al.*, (2024), arXiv:2404.14286 [gr-qc].
- [34] M. Dax, S. R. Green, J. Gair, J. H. Macke, A. Buonanno, and B. Schölkopf, *Physical Review Letters* **127** (2021), 10.1103/physrevlett.127.241103.
- [35] A. Bohé *et al.*, *Phys. Rev. D* **95**, 044028 (2017), arXiv:1611.03703 [gr-qc].
- [36] R. Cotesta, A. Buonanno, A. Bohé, A. Taracchini, I. Hinder, and S. Ossokine, *Physical Review D* **98** (2018), 10.1103/physrevd.98.084028.
- [37] A. Ramos-Buades, A. Buonanno, M. Khalil, and S. Ossokine, *Physical Review D* **105** (2022), 10.1103/physrevd.105.044035.
- [38] M. Khalil, A. Buonanno, J. Steinhoff, and J. Vines, *Physical Review D* **104** (2021), 10.1103/physrevd.104.024046.
- [39] I. Romero-Shaw, J. Stegmann, H. Tagawa, D. Gerosa, J. Samsing, N. Gupte, and S. R. Green, “Gw200208_222617 as an eccentric black-hole binary merger: properties and astrophysical implications,” (2025), arXiv:2506.17105 [astro-ph.HE].
- [40] H. L. Iglesias, J. Lange, I. Bartos, S. Bhambik,

- R. Gamba, V. Gayathri, A. Jan, R. Nowicki, R. O’Shaughnessy, D. M. Shoemaker, R. Venkataraman, and K. Wagner, *Astrophysical Journal* **972**, 65 (2024), arXiv:2208.01766 [gr-qc].
- [41] A. Nagar, S. Bernuzzi, W. D. Pozzo, G. Riemschneider, S. Akcay, G. Carullo, P. Fleig, S. Babak, K. W. Tsang, M. Colleoni, F. Messina, G. Pratten, D. Radice, P. Retteno, M. Agathos, E. Fauchon-Jones, M. Hannam, S. Husa, T. Dietrich, P. Cerdá-Duran, J. A. Font, F. Pannarale, P. Schmidt, and T. Damour, *Phys. Rev. D* **98** (2018), 10.1103/physrevd.98.104052.
- [42] A. Nagar, A. Bonino, and P. Retteno, *Phys. Rev. D* **103**, 104021 (2021), arXiv:2101.08624 [gr-qc].
- [43] S. Albanesi, A. Placidi, A. Nagar, M. Orselli, and S. Bernuzzi, *Phys. Rev. D* **105**, L121503 (2022), arXiv:2203.16286 [gr-qc].
- [44] J. Lange, R. O’Shaughnessy, and M. Rizzo, arXiv e-prints, arXiv:1805.10457 (2018), arXiv:1805.10457 [gr-qc].
- [45] J. Healy, C. O. Lousto, J. Lange, and R. O’Shaughnessy, *Phys. Rev. D* **102**, 124053 (2020), arXiv:2010.00108 [gr-qc].
- [46] J. Healy and C. O. Lousto, *Phys. Rev. D* **102**, 104018 (2020), arXiv:2007.07910 [gr-qc].
- [47] K. Chatziioannou *et al.*, *Phys. Rev. D* **100**, 104015 (2019), arXiv:1903.06742 [gr-qc].
- [48] G. Lovelace *et al.*, *Class. Quant. Grav.* **33**, 244002 (2016), arXiv:1607.05377 [gr-qc].
- [49] V. Gayathri, J. Healy, J. Lange, B. O’Brien, M. Szczepanczyk, I. Bartos, M. Campanelli, S. Klimenko, C. O. Lousto, and R. O’Shaughnessy, *Nature Astron.* **6**, 344 (2022), arXiv:2009.05461 [astro-ph.HE].
- [50] R. Gamba, M. Breschi, G. Carullo, S. Albanesi, P. Retteno, S. Bernuzzi, and A. Nagar, *Nature Astronomy* **7**, 11–17 (2022).
- [51] D. Chiamello and A. Nagar, *Phys. Rev. D* **101**, 101501 (2020), arXiv:2001.11736 [gr-qc].
- [52] J. Healy, C. O. Lousto, Y. Zlochower, and M. Campanelli, *Classical and Quantum Gravity* **34**, 224001 (2017).
- [53] J. Healy, C. O. Lousto, J. Lange, R. O’Shaughnessy, Y. Zlochower, and M. Campanelli, *Physical Review D* **100** (2019), 10.1103/physrevd.100.024021.
- [54] J. Healy and C. O. Lousto, *Physical Review D* **102** (2020), 10.1103/physrevd.102.104018.
- [55] J. Healy and C. O. Lousto, *Physical Review D* **105** (2022), 10.1103/physrevd.105.124010.
- [56] Y. Zlochower, J. G. Baker, M. Campanelli, and C. O. Lousto, *Phys. Rev. D* **72**, 024021 (2005), arXiv:gr-qc/0505055.
- [57] Y. Zlochower, M. Ponce, and C. O. Lousto, *Phys. Rev. D* **86**, 104056 (2012), arXiv:1208.5494 [gr-qc].
- [58] S. Brandt and B. Brügmann, *Phys. Rev. Lett.* **78**, 3606 (1997), gr-qc/9703066.
- [59] M. Ansorg, B. Brügmann, and W. Tichy, *Phys. Rev. D* **70**, 064011 (2004), gr-qc/0404056.
- [60] J. Thornburg, *Class. Quant. Grav.* **21**, 743 (2004), gr-qc/0306056.
- [61] A. Ashtekar and B. Krishnan, *Living Rev. Rel.* **7**, 10 (2004), gr-qc/0407042.
- [62] M. Campanelli, C. O. Lousto, Y. Zlochower, B. Krishnan, and D. Merritt, *Phys. Rev. D* **75**, 064030 (2007), gr-qc/0612076.
- [63] E. Schnetter, S. H. Hawley, and I. Hawke, *Class. Quant. Grav.* **21**, 1465 (2004), gr-qc/0310042.
- [64] C. O. Lousto and J. Healy, *Phys. Rev. Lett.* **125**, 191102 (2020), arXiv:2006.04818 [gr-qc].
- [65] M. Campanelli and C. O. Lousto, *Phys. Rev. D* **59**, 124022 (1999), arXiv:gr-qc/9811019 [gr-qc].
- [66] C. O. Lousto and Y. Zlochower, *Phys. Rev. D* **76**, 041502(R) (2007), gr-qc/0703061.
- [67] H. Nakano, J. Healy, C. O. Lousto, and Y. Zlochower, *Phys. Rev. D* **91**, 104022 (2015), arXiv:1503.00718 [gr-qc].
- [68] G. Ficarra and C. O. Lousto, *Phys. Rev. D* **111**, 044015 (2025), arXiv:2409.18728 [gr-qc].
- [69] A. Ciarfella, J. Healy, C. O. Lousto, and H. Nakano, *Phys. Rev. D* **106**, 104035 (2022), arXiv:2206.13532 [gr-qc].
- [70] J. Healy and C. O. Lousto, *Phys. Rev. D* **105**, 124010 (2022), arXiv:2202.00018 [gr-qc].
- [71] T. Damour, *Phys. Rev. D* **64**, 124013 (2001), arXiv:gr-qc/0103018.
- [72] J. Healy and C. O. Lousto, *Phys. Rev. D* **97**, 084002 (2018), arXiv:1801.08162 [gr-qc].
- [73] D. Wysocki, R. O’Shaughnessy, J. Lange, and Y.-L. L. Fang, *Physical Review D* **99** (2019), 10.1103/physrevd.99.084026.
- [74] J. Wofford, A. B. Yelkar, H. Gallagher, E. Champion, D. Wysocki, V. Delfavero, J. Lange, C. Rose, V. Valsan, S. Morisaki, J. Read, C. Henshaw, and R. O’Shaughnessy, *Phys. Rev. D* **107**, 024040 (2023).
- [75] K. J. Wagner, R. O’Shaughnessy, A. Yelkar, N. Manning, D. Fernando, J. Lange, V. Tiwari, A. Fernando, and D. Williams, “Narrowing rift: Focused simulation-based-inference for interpreting exceptional gw sources,” (2025), arXiv:2505.11655 [astro-ph.IM].
- [76] A. Buonanno and T. Damour, *Phys. Rev. D* **59** (1999), 10.1103/physrevd.59.084006.
- [77] M. A. Shaikh, V. Varma, H. P. Pfeiffer, A. Ramos-Buades, and M. van de Meent, “Defining eccentricity for gravitational wave astronomy,” (2023), arXiv:2302.11257 [gr-qc].
- [78] L. S. Collaboration, V. Collaboration, and K. Collaboration, “Gwtc-3: Compact binary coalescences observed by ligo and virgo during the second part of the third observing run — parameter estimation data release,” (2023).
- [79] P. Peters, *Phys. Rev.* **136**, B1224 (1964).
- [80] L. E. Kidder, *Phys. Rev. D* **52**, 821 (1995), gr-qc/9506022.
- [81] H.-S. Cho, E. Ochsner, R. O’Shaughnessy, C. Kim, and C.-H. Lee, *Phys. Rev. D* **87**, 024004 (2013), arXiv:1209.4494 [gr-qc].
- [82] L. S. Collaboration and V. Collaboration, “Gwtc-2.1: Deep extended catalog of compact binary coalescences observed by ligo and virgo during the first

- half of the third observing run - parameter estimation data release,” (2022).
- [83] M. d. L. Planas, A. Ramos-Buades, C. García-Quirós, H. Estellés, S. Husa, and M. Haney, (2025), arXiv:2504.15833 [gr-qc].
- [84] J. Healy, C. O. Lousto, H. Nakano, and Y. Zlochower, Class. Quant. Grav. **34**, 145011 (2017), arXiv:1702.00872 [gr-qc].
- [85] A. Ciarfella, J. Healy, C. O. Lousto, and H. Nakano, Phys. Rev. D **110**, 084031 (2024), arXiv:2406.11564 [gr-qc].